Planetary and Space Science 254 (2024) 105997

Contents lists available at ScienceDirect

Planetary and Space Science

journal homepage: www.elsevier.com/locate/pss

Performance evaluation of pansharpening for planetary exploration: A case study on the implementation of TGO CaSSIS with MRO HiRISE

A. Tullo [a,*], C. Re [a], G. Cremonese [a], E. Martellato [a], R. La Grassa [a], N. Thomas [b]

[a] INAF, Osservatorio Astronomico di Padova, Vicolo dell'Osservatorio, 5, Padova, Italy
[b] Physikalisches Institut, Sidlerstr. 5, University of Bern, CH-3012, Bern, Switzerland

1. ABSTRACT

The present study analyses the potential of pansharpening algorithms for planetary exploration studies, testing their performance with the 4-band images from the Colour and Stereo Surface Imaging System (CaSSIS) aboard the Exomars 2016 Trace Grace Orbiter (TGO) using HiRISE images from the Mars Reconnaissance Orbiter (MRO) mission as the base. Due to the lack of suitable open-source tools, a suite of scripts was developed to improve alignment between images and enable different component substitution (CS) pansharpening algorithms. The tools developed were tested on a database of images encompassing several regions of Mars to explore its vast diversity in colours, tones, and textures. Then, the resulting images were investigated using spectral and structural performance indices, comparing the results with the source images and the colour information from the HiRISE central channels.

The results show that a substantial number of the tested algorithms are more than suitable for data enhancement, showing a considerable improvement in the structural characteristics of the images without sacrificing their spectral characteristics. In detail, the Gram-Schmidt method, widely used in terrestrial pansharpening, turns out to be the best compromise among the tested algorithms. Regarding the other tested algorithms, GIHS and the MMSE Brovey, a modified version of the classic Brovey, show the most significant increase in structural properties, while GHPF and GHPM show the interesting ability to maintain virtually unchanged spectral conditions of the multispectral source data.

In addition, the analysis reveals the applicability of pansharpening at a ground resolution increment up to 18 times, from 4.5 up to 0.25 m/px, a broader range than is usually used in traditional pansharpening.

1. Introduction

Remote sensing images represent one of the main tools of planetary exploration, on which studies of all kinds are based, from mineralogical and morphological analyses to three-dimensional surface topography reconstruction.

Multispectral Sensors allow the compositional properties of the surface to be probed by sampling radiant light through multiple bands characterised by a narrow spectral range. Given the limited portion of the spectrum, multispectral sensors need large apertures and reduced spatial resolutions to capture the necessary amount of radiant energy while keeping acquisition times within an acceptable range. In this way, an adequate signal-to-noise ratio can be obtained. A panchromatic acquisition mode (PAN) trades spectral information, acquired through a single larger band, with the capacity for denser surface sampling (a reduced ground sampling distance – GSD). Despite modern technological developments, low-orbit planetary instruments usually require a trade-off between spatial and spectral resolution (Thomas et al., 2008).

An alternative approach used by some missions, is to use both multispectral and high-spatial resolution PAN instruments, in a complementary manner. Of course, it is also possible to fly the two types of instruments on completely different missions to the same target. Pansharpening, or pan-sharpening, data fusion techniques take advantage of such a combination to produce spatially enhanced multispectral images (Ciotola et al., 2022.

Several studies show how pansharpening results are beneficial for numerous fields, including photointerpretation (Kaur et al., 2021), feature extraction and classification (Bruzzone et al., 2006; Castillejo--González, 2018), spectroscopy (Du et al., 2007), target detection and time-variation monitoring (Bovolo et al., 2010; Zhang, 2010) . Although this practice is widely established and studied in the field of Earth-observing (EO) remote sensing, different complications and the lack of accessible tools have meant that pansharpening is rarely used in planetary exploration. When used, pansharpening has shown appreciable advantages for morphological analysis Kwan et al., 2017; Semenzato et al., 2020; Lucchetti et al., 2021) and image simulation (Tornabene et al., 2018).

In this paper, an evaluation of the performance of different Component Substitution (CS) (Shettigara, 1992) pansharpening techniques applied to the implementation of ExoMars TGO CaSSIS colour

* Corresponding author.
E-mail address: adriano.tullo@inaf.it (A. Tullo).

https://doi.org/10.1016/j.pss.2024.105997
Received 26 March 2024; Received in revised form 24 September 2024; Accepted 5 November 2024
Available online 9 November 2024

Table 1
Spectral properties of CaSSIS [Pommerol et al., 2022] and HiRISE [McEwen et al., 2007; Delamere et al., 2010] instruments.

Filter	Effective Central Wavelength [nm]	Approximate spectral range [nm]
CaSSIS		
Blue-Green	495	425–560
Pan	678	560–795
Red	836	785–885
Near-Infrared	939	880–1000
HiRISE		
Blue-Green	536	400–580
Red	694	570–830
Near-infrared	874	790–1100

images with MRO HiRISE is reported.

2. Test dataset

2.1. Instruments

We selected images of the Colour and Stereo Surface Imaging System (CaSSIS) and High Resolution Imaging Science Experiment (HiRISE) instruments onboard the ESA ExoMars Trace Gas Orbiter (TGO) (Thomas et al., 2017) and NASA Mars Reconnaissance Orbiter (MRO) (McEwen et al., 2007) missions, respectively. These instruments are specifically suitable for the analysis because of several factors, including the fact that they are the highest spatial resolution sensors to date in Mars orbit except for the past Mars Orbital Camera (MOC) (Malin et al., 1992).

CaSSIS produces high-resolution multispectral images of Mars in four bands, spanning the blue, visible, and near Infrared wavelength range (Table 1). The instrument uses a square 2k CMOS sensor mounted at the focus of a 4-mirror off-axis telescope with 875 mm effective focal length (Pommerol et al., 2022). It enables radiometrically calibrated surface colour/spectral observations up to 4.5 m/px GSD from a circular 400 km orbit. By implementing a "push-frame" approach, the individual acquisitions (or "framelets") compose observations ~ 9 km wide by 30–40 km long.

HiRISE is the highest-resolution orbital camera ever sent to Mars, achieving a GSD of 0.25–0.5 m/px. Being based on the "push-broom" approach, the instrument consists of independent CCD sensors attached to a 0.5-m aperture telescope for an effective focal length of 12 m. Ten of the fourteen CCDs permit the acquisition of a significant 300 nm bandwidth portion of the visible and NIR spectrum, centred in the red portion at ~700 nm. This band, commonly referred to as RED, acts similarly to a panchromatic sensor and allows observations with a swath width of 6 km. In addition, the HiRISE instrument also includes a narrow middle portion (about 1.2 km wide) where two other bands are acquired, comprising the lower part of the visible spectrum (BLUE-GREEN) and a portion of the Near-Infrared (IR) (Table 1). Since the HiRISE and CaSSIS spectral ranges mostly overlap each other, the comparison of the CaSSIS-derived pansharpened products and the HiRISE colour images could provide the opportunity for further evaluation.

The scale ratio between the CaSSIS and HiRISE images (ranging from 9 to 18x) also poses an interesting challenge to pansharpening techniques. Although there is no upper limit for the scale ratio, values around 4x to 8x are typical in Earth-Observing applications (Cheng and Chaapel, 2010; Tu et al., 2012; Alcaras et al., 2021). The footprint overlap of data from the two sensors is a common occurrence for areas of high scientific interest. It may also be requested, as acquisitions for both instruments are target-driven based on community suggestions.

2.2. Selected images

To ensure statistical significance, the test dataset consists of selected images in different geological contexts, sampling different regions of Mars (Fig. 1). This allows the variation of results to be observed in the context of Mars's colour diversity and within a range of differing tones and textures.

For the same reason, the images selected are taken at distinct times of

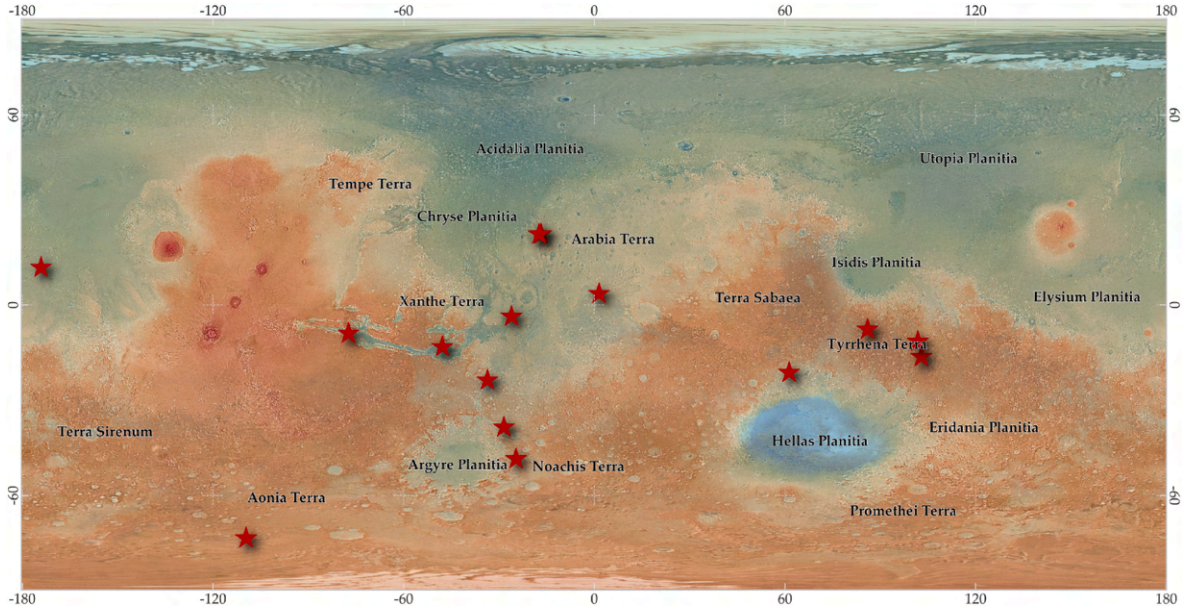

Fig. 1. The positions of the images that compose the test dataset on the Martian surface are marked as red stars. The images were chosen to represent a wide range of geological contexts, contrast, colours, and lighting conditions. The basemap shows MOLA elevation on the Mars Viking Colorized Global Mosaic (Mars, 2000 Equidistant Cylindrical projection).

Table 2
List of image pairs used as test dataset, location, and acquisition details. The coordinates refer to the central point of the CaSSIS images. All selected HiRISE images overlap more than 80% of the reference CaSSIS image.

Region	Latitude [°]	Longitude [°]	CaSSIS Id	Emission [°]	Incidence [°]	Phase [°]	North Azimuth [°]	SubSolar Azimuth [°]	HiRISE Id	Emission [°]	Incidence [°]	Phase [°]	North Azimuth [°]	SubSolar Azimuth [°]
Aureum Chaos	−3.808	333.683	MY36_015213_184_0	14.6	66.9	69.3	270.0	343.1	ESP_074351_1765	3.3	53	56.4	97	341.2
Vallis Marineris	−9.157	282.792	MY36_014991_189_0	14.6	21.1	11.5	270.0	287.6	PSP_007443_1705	10	50	42.1	96	34.7
Pettit Crater	11.879	185.902	MY36_014845_169_0	9.1	25.6	27.8	270.0	175.2	PSP_001882_1920	4.3	53	48.6	97	11
Capri Mensa	−13.134	312.268	MY34_002326_346_2	13.6	26.6	31.7	270.0	201.8	ESP_022553_1665	16.4	36	20.6	95	344.8
Meridiani Planum	3.708	1.481	MY36_017861_177_1	14.3	25.4	24.1	270.0	322.8	ESP_052893_1835	3.2	49	46.8	97	37.2
Mawrth Vallis	22.339	343.198	MY34_004209_158_0	13.8	49.9	61.8	270.0	109.9	PSP_010394_2025	2.8	51	48.4	97	7.9
Mawrth Vallis	22.087	342.83	MY36_016518_157_0	14.4	48.7	49.2	270.0	345.8	ESP_051153_2025	19.2	35	54.2	97	351.4
Kenge Crater. Tyrrhena	−16.363	102.951	MY34_004795_342_1	13.6	26.7	25.6	270.0	169.9	ESP_012315_1635	17.1	54	36.8	97	355
Tyrrhena Terra	−9.882	86.95	MY35_012250_189_0	7.5	18.3	16.4	270.0	112.2	ESP_058442_1720	3.5	31	27.5	97	350.7
Lau Crater. Australe	−73.36	250.306	MY36_019484_262_2	13.9	63.7	57.5	160.4	162.5	ESP_073537_1065	0.3	74	74.2	101	30
Eberswalde Crater	−23.825	326.417	MY34_004011_206_1	14.5	78.9	85.3	270.0	157.7	PSP_001336_1560	0.3	67	67.2	97	39.8
Hesperia Planum	−11.586	101.856	MY36_019052_194_0	9.4	52.0	50.9	270.0	187.5	ESP_033202_1685	3	41	43.5	97	28.2
Wirtz Crater	−48.527	335.357	MY36_019629_231_0	15.3	74.0	76.0	270.0	1.0	ESP_011911_1310	4.3	62	65.8	97	22.2
Nereidum Montes	−38.49	331.489	MY36_019318_220_0	15.2	32.7	24.3	270.0	281.4	ESP_069433_1410	9.2	77	70.7	97	43.1
Hellas North Border	−21.24	61.371	MY34_002260_337_0	13.6	44.4	47.9	270.0	201.5	ESP_012989_1585	3.8	44	40.4	97	352

the day and under different illumination conditions. This allows us to assess the impact of different acquisition conditions on the quality of the output products. Clips were extracted from the images, which were pre-processed and aligned to exclude edge areas and null pixels to avoid errors commonly associated with them. On average, the 25 clips extracted from the CaSSIS data are 1500 px per side, totalling about 50 million CaSSIS pixels processed through >600 million HiRISE pixels. The resulting dataset consists of approximately 800 GB of pansharpened images.

Table 2 shows a list of the source images used and their details.

2.3. Preprocessing and alignment

The CaSSIS images used for the study were retrieved from the archive of the University of Bern (observations.cassis.unibe.ch) as already radiometrically corrected and mosaicked ISIS cubes (Kirk et al., 2008; Re et al., 2019; Re et al., 2022; Perry et al., 2022). The mosaicking of the CaSSIS data includes also the improvement of the framelets camera pointing information through bundle adjustment. This is realized through the ISIS Jigsaw software (Laura et al., 2023), which exploits the overlapping portion of individual frames to correct the misalignments (Re et al., 2019; Re et al., 2022). After being mosaicked separately, the individual bands are map-projected, aligned with each other, and joined together as a multispectral cube.

HiRISE images were instead pre-processed from raw data in ISIS according to commonly used procedures (Kirk et al., 2008): the individual HiRISE channels are converted to ISIS cubes and radiometrically calibrated before being co-registered and stitched together. The mosaicked images are then normalised, destriped, and map-projected (Kirk et al., 2008).

Before applying pansharpening radiometric transformations, it is crucial to ensure that the two images are accurately aligned. This step is generally performed manually with the Georeferencing tools provided by the GIS programs QGIS and ArcGIS. The process is time-consuming and can be prone to errors caused by the operator. To simplify this step and mitigate the possibility of errors, an automatic pre-alignment methodology based on automatic search for tie points and the estimation of projective transformations was developed and applied.

The process involves the implementation of the SIFT ("Scale-invariant feature transform") computer vision algorithm (Lowe, 1999), inherited from the photogrammetric and stereogrammetric fields, in order to detect and match interest points (recognisable features) between the images. It can identify significantly more tie points than a human operator and, based on these, the developed tool computes a homographic transformation to align the HiRISE image to the corresponding CaSSIS (Fig. 2). In this way, PAN and MS view geometries can be harmonized without, or with the bare minimum, risk of distortions and warping.

The implementation of SIFT used is derived from the OpenCV library (Bradski, 2000 - v. 4.9), to which no optimisations related to the surface of Mars have been made other than calibrating the contrast thresholds for the detection of interest points. The number of detected matches can vary from a few hundred to more than a thousand, depending on the quality of the images and their textural characteristics.

In addition, the identification of well-distributed points across the images ensures a better definition of the homography. For this reason, the user is allowed to reiterate the process to find more points targeting the process to specific regions of the images through masks, for example, to refine the search in areas previously poorly considered.

On the preliminary aligned images, the operator applies local enhancements through GIS tools to compensate for the misalignments derived from topographic elements that the homographic projection does not handle. The procedure reduces co-registration time considerably and permits pixel-level accuracy for the CaSSIS data (Fig. 3). The possibility of a certain margin of error still cannot be excluded, particularly in areas where the lighting conditions do not allow common

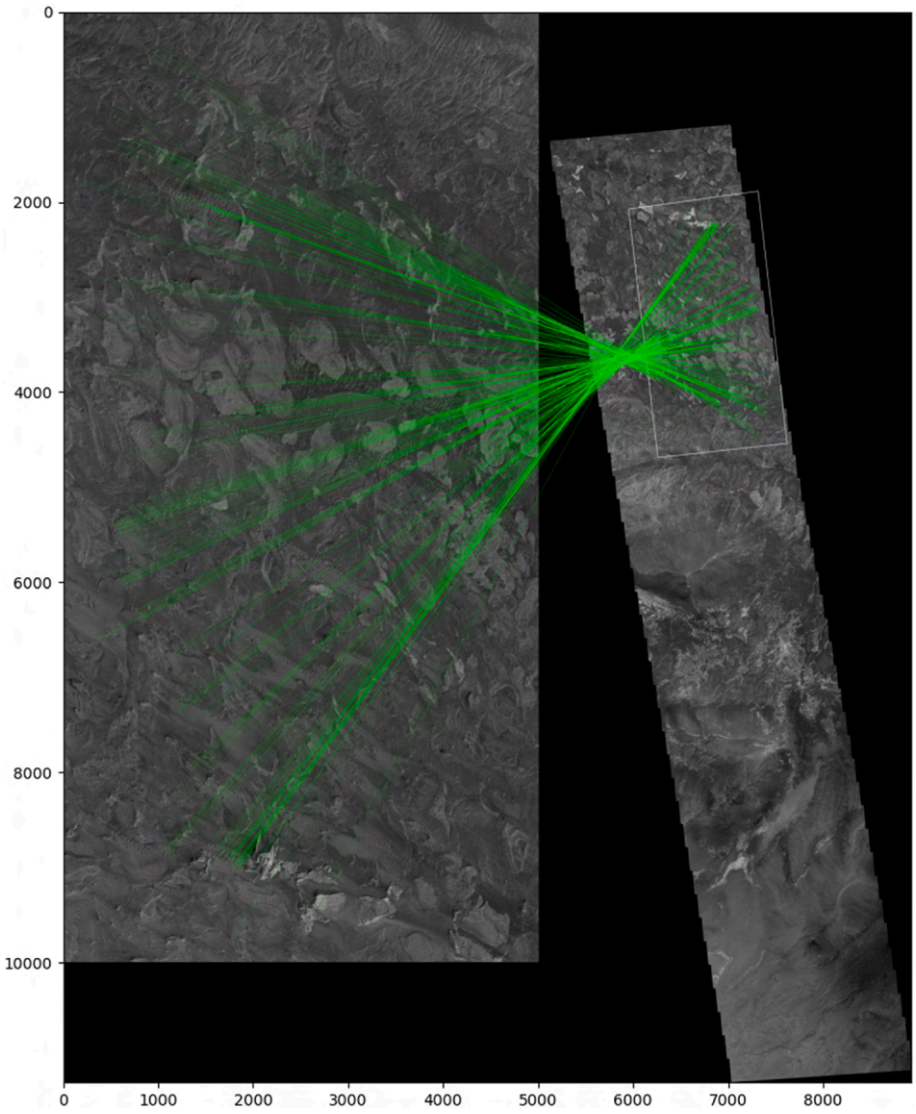

Fig. 2. Example of HiRISE image (PSP_007443_1705 on the left) aligned to a reference CaSSIS image (MY36_014991_189, on the right) through matching points between images (linked in green) acquired by SIFT operator through which the homographic projection that best approximates the position of the points is calculated. In the image on the right, the resulting HiRISE footprint is shown in white.

points between images to be defined with certainty.

3. Pansharpening algorithms tested

Over more than four decades of development, an increasing number of pansharpening techniques have been developed on the basis of quite different approaches (Alparone et al., 2007; Loncan et al., 2015; Meng et al., 2021). To date, pansharpening plays an essential role in the enhancement of remote sensing data (e.g. Alparone et al., 2015). Recent classification efforts such as Vivone et al., 2021 have divided these techniques into four large families: Component Substitution (CS), Partial Replacement Adaptive Component Substitution (MRA), Variational Optimization-Based Techniques (VO), and Machine/Deep Learning (ML).

Among these, CS methods are generally considered the most traditional and well-established. They are based on pixel-wise transformation in which the multispectral data (MS) image space is projected into the panchromatic data (PAN) dimension and then moulded according to different radiometric fusion principles (Vivone et al., 2015). Despite the recent emergence of more articulated techniques, CS-based methods remain of significant use and interest due to their ease of use and implementation and low computational cost (Palubinskas, 2013). Traditionally, such methods have been considered to suffer from alteration in the spectral response and its slope, but the development of more modern techniques shows that this problem is now commonly minimised (Aiazzi et al., 2007; Palubinskas, 2013; Li et al., 2020; Li and Yang, 2011; Vicinanza et al., 2015).

Different MRA methods, such as Laplacian pyramids (Aiazzi et al., 2012), further minimise spectral deformation problems, but several studies show that they are susceptible to misregistration between MS and PAN data. As discussed in the previous chapter, this is only sometimes negligible in the case of aligning images acquired from different instruments at different times and with different acquisition geometries. In contrast to the more recent MRA and VO methods (Garzelli, 2016; Jin et al., 2022), the relative computational simplicity and wide optimization margin allow CS-based methods to be useable in contexts with large datasets and demanding number formats (usually float32 or 64), such as those commonly handled in planetary exploration, keeping processing times within acceptable margins (Aiazzi et al., 2007). According to our tests, performed on an Intel Xeon w7-2475X (20-Core) processor,

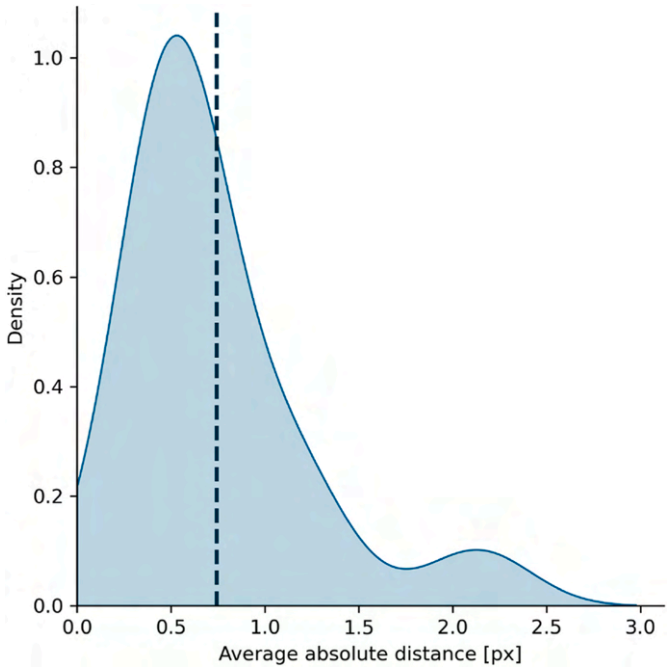

Fig. 3. Indicative measure of the alignment procedure accuracy achieved by comparing the absolute distance, in CaSSIS pixels, between points identified in the MS image and the PAN aligned to it. The analysis was conducted on the entire test dataset through SIFT algorithm after alignment procedure, considering a statistically significant number of matching points (≈850 on average).

processing takes 2–8 min per image, depending on size and method. Furthermore, since they are based on algorithms repeated equally for each pixel, they do not require vast training datasets like AI-based techniques to adapt the method to the context, which is rarely available and complex to implement in fields other than Earth-observing (Deng et al., 2022; Huang et al., 2015; Xu et al., 2017).

Due to the lack of open-source or commercial tools adaptable to the purpose, dedicated tools have been developed for each pansharpening method. The tools were programmed in Python using open-source libraries, including GDAL, Numpy, Numba, Scipy, and Scikit. In its final version, the toolbox will be distributed open source.

As several methods do not allow more than three bands, combinations of CaSSIS NIR-PAN-BLU and RED-PAN-BLU bands were used in equal numbers for all methods tested. Fig. 4 shows an example from the test dataset of applying the chosen methods, as described below.

3.1. Brovey-based methods

Brovey is one of the most widely used methods, introduced as early as 1983 in Hallada and Cox, 1983. The Brovey method and its derivatives are based on the chromaticity transform, where the three MS band components (usually referred to as RGB) are normalised, divided from a pseudo-panchromatic (I) derived from the summed MS bands, and multiplied by the original panchromatic image (Liu, 2000; Aiazzi et al., 2007). Weighted versions of the method differentiate the contributions of individual MS bands using specific weight coefficients (w) and thus allow range differences between MS and PAN data to be considered and preserved.

$$I = \frac{\sum_{k=1}^{nb} w_k * MS_k^{LR}}{\sum_{k=1}^{nb} w_k} \quad (1)$$

$$MS^{HR} = \frac{PAN}{I} * MS^{LR} \quad (2)$$

The weights can be deduced from the analysis of the spectral radiance response of the two instruments, comparing the intercepted radiance between the panchromatic and multispectral bands for every wavelength interval (Parente and Pepe, 2017) , or can be approximated by statistical operations. Of this second type, the "Brovey MMSE" method tested in this study is inspired by the methods of Garzelli et al., 2008 and Garzelli, 2014, in which the weights are established utilising a minimum mean square error (MMSE) estimator algorithm.

3.2. IHS-based methods

The Intensity, Hue and Saturation Transformation (IHS), introduced by Carper et al., 1990, is based on an initial definition of spatial (Intensity) and spectral (Hue and Saturation) information from an initial three-band MS image (Haydn, 1982).

The image is then reconstructed at the target resolution by replacing the intensity component (I) with the PAN while keeping the other two components unchanged.

$$I = \sum_{k=1}^{nb} \alpha * MS_k^{LR} \quad (3)$$

$$\alpha = \frac{1}{nb} \quad (4)$$

$$MS^{HR} = MS^{LR} + (PAN - I) \quad (5)$$

In the generalized version (GIHS) (Aiazzi et al., 2007), the intensity component, I, from the low-resolution MS bans is instead replaced with histogram-matched high-resolution PAN information before finally reinverting the process, thus preserving the original range of values.

$$PAN_{hm} = \frac{\sigma I}{\sigma PAN} (PAN - \mu PAN) + \mu I \quad (6)$$

3.3. High-pass methods

The principle of the High-Pass (HP) family of methods is to exploit the high-frequency information from the high-resolution PAN image, or a normalised version, and add it to the over-sampled MS image (Chavez et al., 1991). The high-frequency information (also defined "details image) is usually computed by filtering the PAN with a low-pass boxcar (uniform) filter and subtracting this from the original PAN. These methods have been studied and are widely used because they permit a bare minimum alteration of the original spectral information.

In the High-Pass Filtering (HPF) methods, the high-frequency information is added directly to the MS image, while in High-Pass Modulation (HPM) types, it is multiplied by modulation coefficients defined by comparison with the intensity of the original MS (Vivone et al., 2014).

3.4. Gram-Schmidt (GS)

The Gram-Schmidt pansharpening method is based on the general Gram-Schmidt vector orthogonalisation. Since its introduction and patent by Laben and Brower, 2000, it has become one of the most popular algorithms because it presents a minimal trade-off in both maximising image sharpness and minimising colour distortion.

The algorithm is based on a forward and backward transformation of

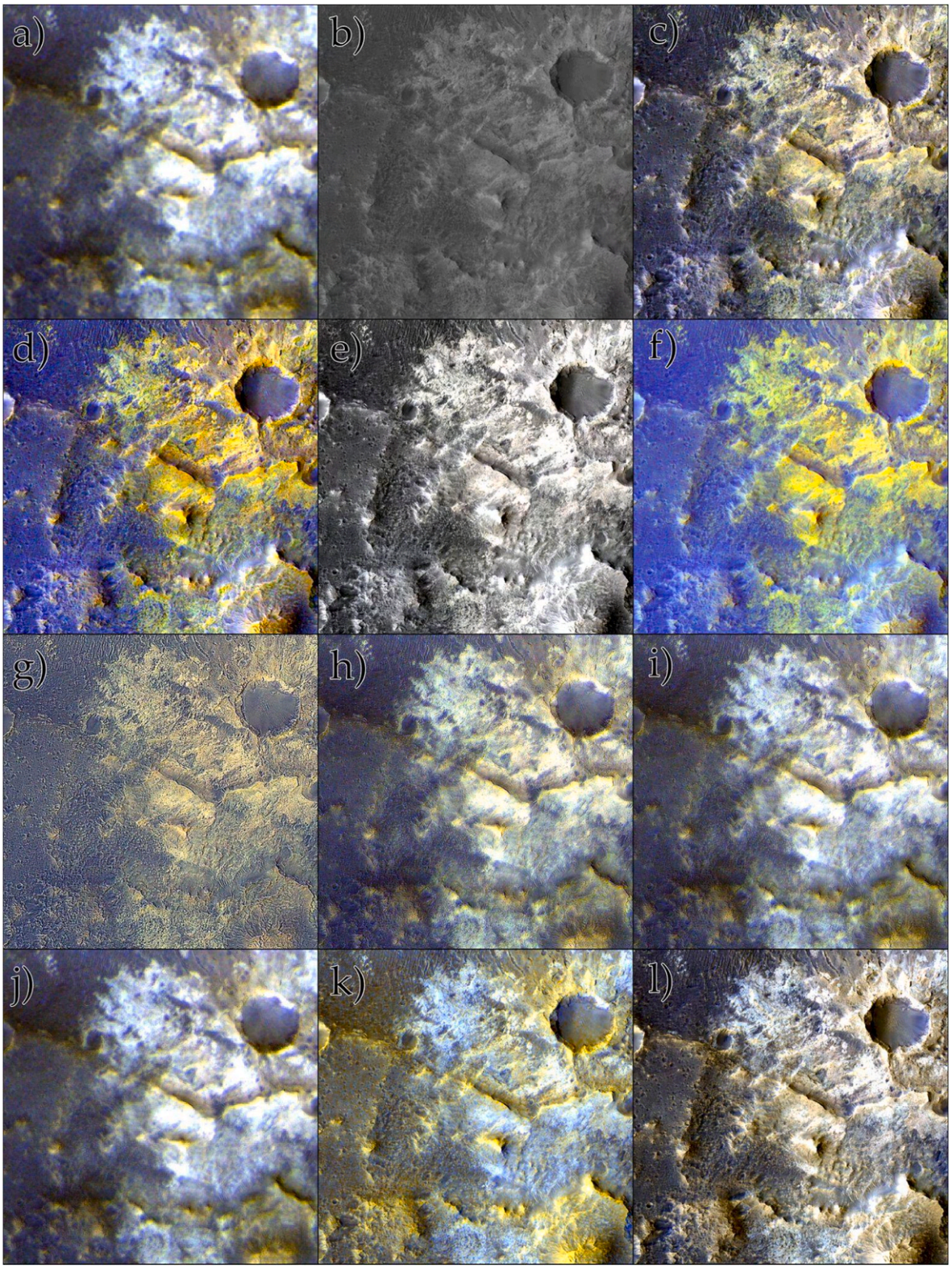

Fig. 4. Overview of the nine pansharpening algorithms tested in the study compared to a) the original CaSSIS MS image (MY34_004209_158_0) and b) the reference HiRISE PAN (PSP_010394_2025): c) equal weights Brovey, d) MMSE Brovey, e) IHS, f) GIHS, g) HPF, h) GHPF, i) HPM, j) GHPM, k) GS, and l) merged RGB colour HiRISE for comparison. Contrast stretching is set at 2% to emphasise visual details. The image depicts part of the Mawrth Vallis valley floor, an area of particular geological interest due to its mineralogical variety. In the area a bright bedrock rich in Fe/Mg-clays outcrops below a darker igneous unit and dust Loizeau et al., 2007.

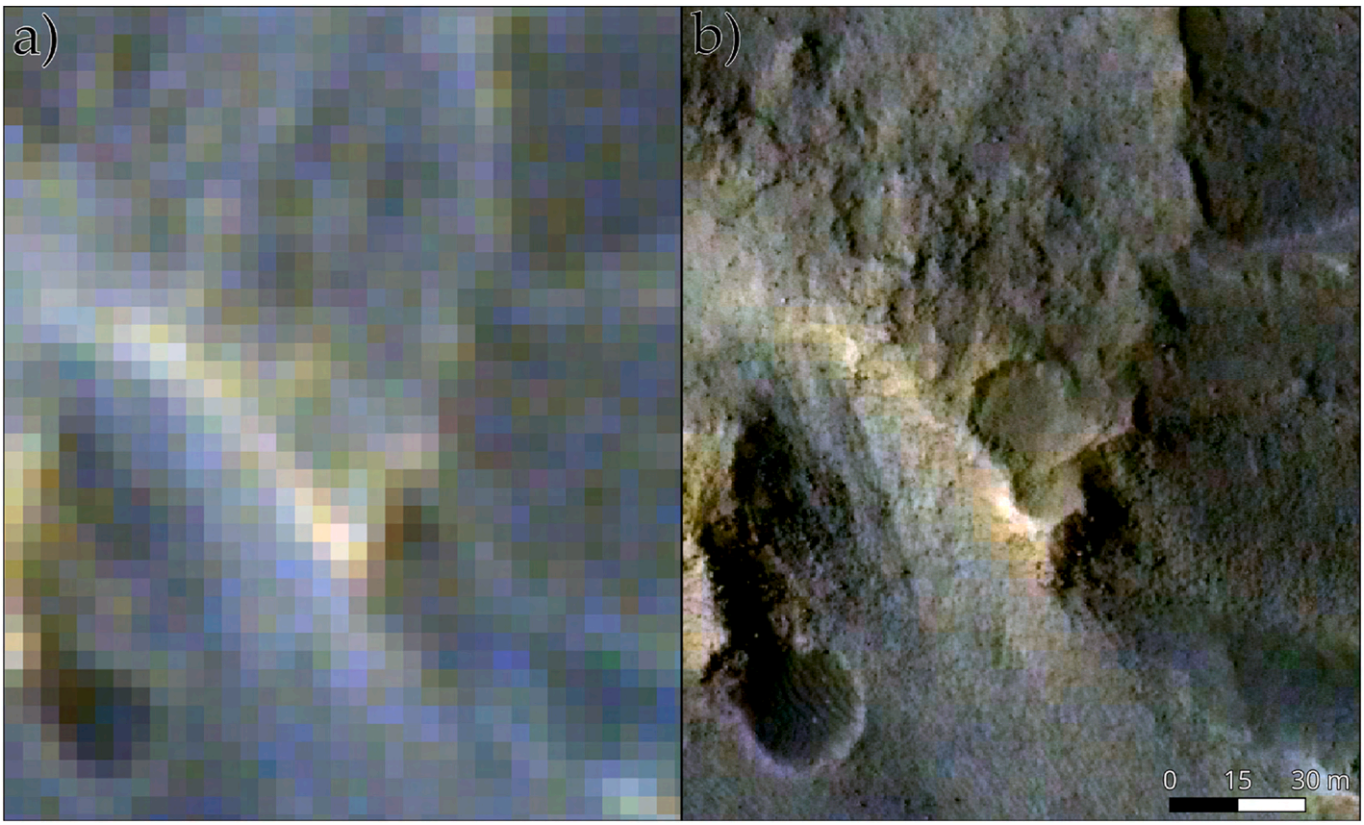

Fig. 5. Detail of the maximum resolution increase obtained during testing, from 4.5 m/px to 0.25 m/px. The image depicts the same area with a) the original CaSSIS image (MY36_014845_169_0 - NIR/PAN/BLU rgb composite) and b) the image pansharpened through an equal weights Brovey algorithm and the HiRISE image PSP_001882_1920. The image depicts the inner part of the central-peak Pettit Crater, east of Orcus Patera and Marte Vallis.

the entire image: the bands are treated as a series of n-dimensional vectors composed of the contributions of individual pixels. They are forward transformed (orthogonalized) on a synthetic pseudo-panchromatic linear combination of the n MS bands and then "rotated" back, performing the inverse transformation replacing the reference vector with the original histogram-matched PAN (Maurer, 2013).

4. Evaluation indexes

An evaluation of the methods makes it possible to assess their strengths and limitations in order to simplify their adoption according to the user's context and purpose. Visual analysis by experienced operators and end users is generally the primary evaluation method for a pan-sharpening algorithm (Scarpa and Ciotola, 2022).

The quality of satellite data is a summa of parameters that can be evaluated both subjectively and objectively. For example, in photointerpretation and cartography, the improvement of the data is mainly perceived by the evidence of details and sharp boundaries. In spectroscopy, data can be enhanced to increase the signal-to-noise ratio and assist endmember extraction processes, keeping the deformation of the original spectrum minimal. Despite this, evaluation indexes represent a further level of verification, allowing the quality of products to be defined numerically and systematically. Applying a mathematical evaluation process also makes it possible to evaluate larger datasets, minimising the statistical error. Because the performance of pan-sharpening algorithms is both spectrally and spatially dependent, the qualities of products are analysed here employing six different indicators referring to spectral preservation and structural image qualities. The main spectral measurements are treated according to the reduced resolution (RR) protocol similar to the approach introduced by Wald et al., 1997 and widely adopted by subsequent authors (e.g. Vivone et al., 2015; Vivone et al., 2021): the method involves subsampling the final products at the original resolution, allowing direct comparison.

Furthermore, the presence of two additional HiRISE bands in the central portion of the images provides an opportunity to compare the final products at full resolution (FR), albeit considering the different nature of the two instruments and the reduced portions of the images. A brief description of the valuation indexes adopted is given below. Unless otherwise indicated, all the parameters are calculated separately per pixel and averaged.

The Spectral Angle Mapper (SAM) is a spectral slope alteration measurement that stands out for its simplicity yet effectiveness (Yuhas et al., 1992). It indicates the angle between the original and the pan-sharpened spectral vectors for each pixel, usually indicated in decimal degrees. Changes in inclination are a sign of alterations in the original spectral shape, so the ideal value is 0. This indicator is widely used because of its sensibility to the spectrum's shape deformations. However, since it is based on ratios, it does not show the eventual joint alterations in the range of values. The formulation for SAM, considering the reference image "r," the transformed image "t", and the number of bands "i", ranging from 1 to "nb", is:

$$SAM(r,t) = cos^{-1}\left(\frac{\sum_{i=1}^{nb} t_i r_i}{\left(\sum_{i=1}^{nb} t_i^2\right)^{\frac{1}{2}}\left(\sum_{i=1}^{nb} r_i^2\right)^{\frac{1}{2}}}\right) \quad (7)$$

The RMSE indicator is another simple measure, focused on the spectral response range rather than the spectral shape. It is calculated

Table 3
Average results of the algorithms tested referring to the entire test dataset. In brackets, the standard deviation. For each evaluation index, the three best results are highlighted in bold. In the box-and-whisker graphs below, the statistical distribution of the tests for each algorithm is shown, highlighting the median (Q2) in red. In the plot, for some spectral indexes Br and IHS methods are not shown because they are out of scale.

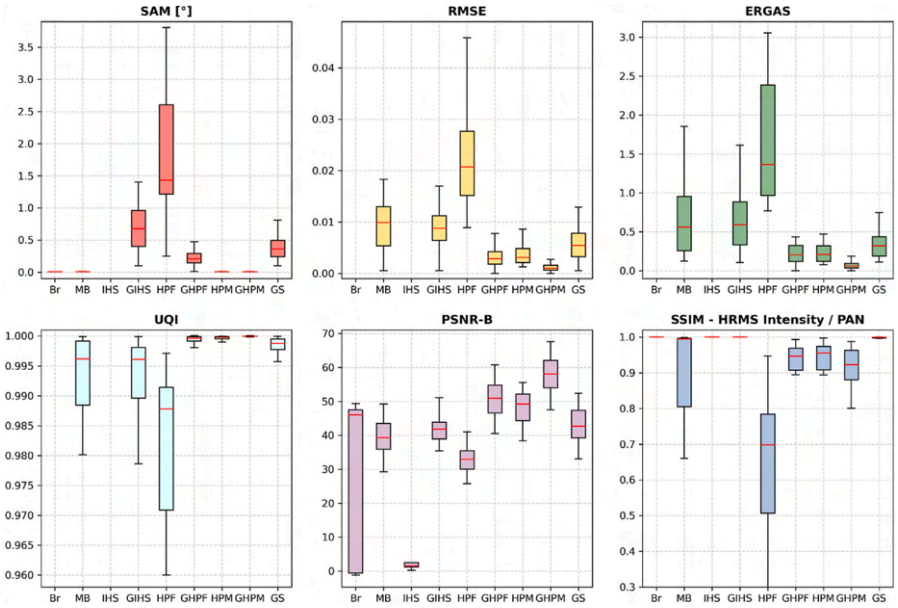

	SAM [°]	RMSE	ERGAS	UQI	PSNRB	SSIM MS (RR)[a]	SSIM PAN (FR)[b]
Brovey	0.012 (0.02)	0.889 (0.058)	70.363 (62.112)	0.086 (0.036)	26.517 (23.957)	0.139 (0.057)	**0.985 (0.069)**
MMSE Brovey	**0.008 (0.001)**	0.013 (0.015)	0.942 (1.371)	0.984 (0.038)	39.738 (8.174)	0.545 (0.196)	0.805 (0.388)
IHS	11.924 (2.12)	0.861 (0.057)	78.61 (67.229)	0.087 (0.036)	9.684 (18.112)	0.138 (0.057)	**0.985 (0.069)**
GIHS	0.81 (0.749)	0.011 (0.012)	0.749 (0.666)	0.99 (0.025)	42.724 (7.573)	0.64 (0.119)	**0.98 (0.077)**
HPF	2.667 (3.805)	0.025 (0.011)	2.382 (3.016)	0.968 (0.056)	32.991 (3.913)	0.473 (0.17)	0.597 (0.344)
GHPF	0.23 (0.145)	**0.004 (0.002)**	**0.256 (0.177)**	**0.999 (0.001)**	**53.24 (13.818)**	0.686 (0.14)	0.907 (0.143)
HPM	**0.008 (0.001)**	**0.004 (0.002)**	**0.24 (0.147)**	**≈ 1 (0)**	**50.179 (9.631)**	0.684 (0.204)	0.908 (0.177)
GHPM	**0.008 (0.001)**	**0.001 (0.001)**	**0.076 (0.052)**	**≈ 1 (0)**	**60.866 (14.421)**	0.907 (0.068)	0.912 (0.074)
Gram-Schmidt	0.431 (0.244)	**0.006 (0.004)**	0.411 (0.428)	**0.998 (0.005)**	43.747 (6.543)	0.6 (0.137)	**0.998 (0.003)**

[a] SSIM index of the comparison between the original and the transformed MS data, conducted at RR.
[b] SSIM index of the comparison between the original PAN data and the pseudo-PAN of the transformed MS data, at FR.

from the difference between the mean values of the original MS image and the pansharpened MS output and its standard deviation, according to the formula:

$$RMSE(r,t) = \sqrt{\Delta\underline{i}^2_{px} + \sigma\Delta\underline{i}^2_{band}} \tag{8}$$

$$\Delta\underline{i} = \mu_r - \mu_t \tag{9}$$

The ideal value is obtained when local and global mean values coincide, in which case the RMSE is 0. The main limitation of RMSE is that errors in each band may not be reflected in the average value of the band itself. This implies that an analysis based on it may deviate significantly from the visual perception of the error, which considers the image in its entirety (E.g. a mean shifted image will be visually indistinguishable from the original image but will have poor RMSE values). The sensitivity to local variations makes RMSE and derived methods particularly useful for highlighting distortions in intensity values, but of little or no value in methods that do not maintain the same range of values (such as non-normalised versions of Brovey and IHS described below).

The ERGAS index, introduced by Ranchin and Wald, 2000, is a normalised dissimilarity indicator encompassing both spectral and structural fidelity (Wald, 2002). Its relatively simple implementation (cf. Eq. (4)) and insensitivity to the number of bands, resolution factor, and spectrum range have made it a widely adopted parameter in pansharpening performance analyses (Alparone et al., 2007). The ERGAS index is defined as:

$$ERGAS(r,t) = 100\, s \sqrt{\frac{1}{nb}\sum_{i=1}^{nb}\left(\frac{RMSE(r_i,t_i)}{\underline{r_i}}\right)^2} \tag{10}$$

Being based on RMSE, lower values indicate better results. ERGAS also inherits from RMSE strengths and, albeit to a lesser extent, limitations (e.g. sensitivity to mean shifting and dynamic range change).

Developed in the same period as ERGAS, the Universal Image Quality Index, abbreviated as UQI, UIQI, or simply Q-index, was advanced by Wang and Bovik, 2002 to overcome the limitations of other evaluation methods, like RMSE and PSNR:

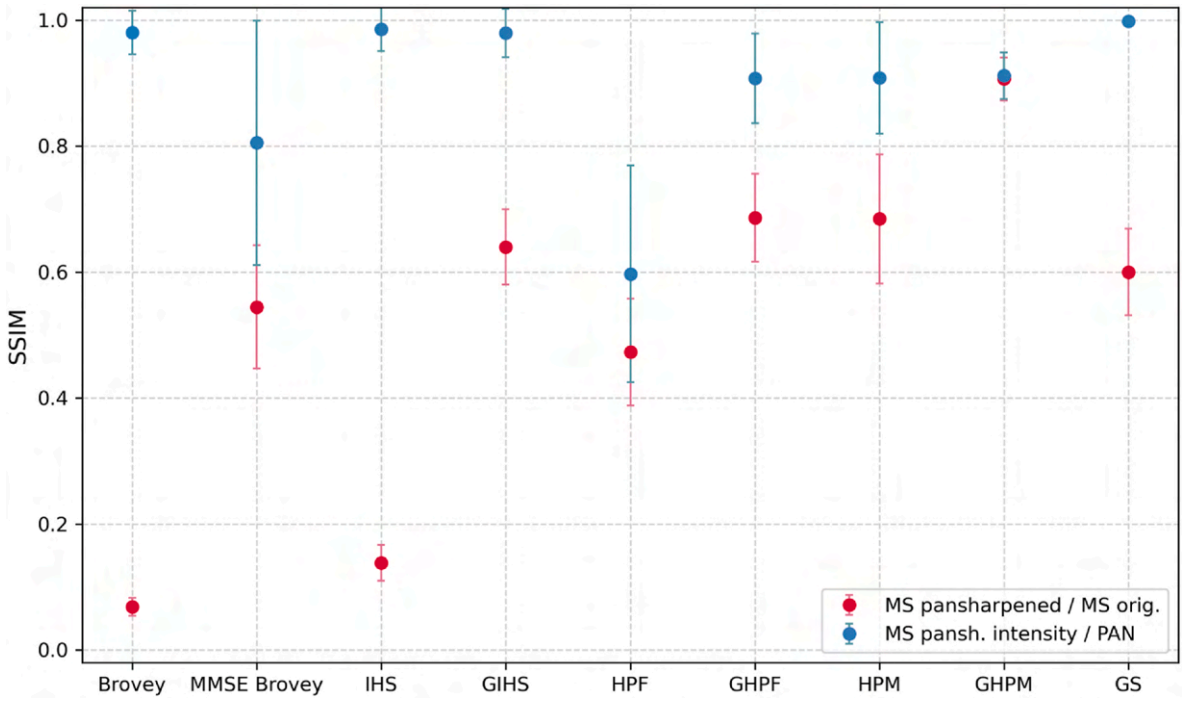

Fig. 6. Comparison of averaged Structural Similarity Image Measure (SSIM) parameters derived from the comparison of the results with the pre-transformation CaSSIS image at RR in red, and with the reference RED HiRISE at FR in blue, listed by method. The parameter analyses the structural properties of the images, whereby the discrepancy between the two values reflects the gain in visual details that ideally match the panchromatic, and the deviation from the original image. The error bars indicate the measured standard deviation for the dataset.

$$UQI_b(r_b, t_b) = \frac{\sigma_{rt}}{\sigma_r \sigma_t} \frac{2\mu_r \mu_t}{\mu_r^2 + \mu_t^2} \frac{2\sigma_r \sigma_t}{\sigma_r^2 + \sigma_t^2} \tag{11}$$

where μ_r and μ_t are the local mean, σ_r and σ_t the standard deviation, and σ_{rt} the cross-covariance. The range of the UQI is from −1 to 1, where 1 represents the ideal value for two identical images. The UQI is suitable for assessing both spectral and structural properties and aligns more closely with human visual perception, making it a better indicator of perceived image quality than previous metrics. Since it is based on global statistical values along the image, it is less sensitive to local variations and, therefore, less suitable for highlighting minor artefacts.

In this respect, the use of the PSNR-B introduced in the study is more suitable. The PSNR-B, which stands for "Peak Signal-to-Noise Ratio with blocking effect factor", is a variant of the classic PSNR introduced by Yim and Bovik, 2011, with the aim to include a measurement of image "blockiness". The blocking artefact is a common error usually observed with image compression or manipulation algorithms based on image subdivision into distinct blocks (Yim and Bovik, 2011; Mastani and Shilpa, 2013). In its simplest form:

$$PSNR - B = 10\, log_{10} \frac{1}{MSE - B} \tag{12}$$

$$MSE - B = MSE(r, t) + \sum_{i=1}^{nb} BEF(t_i) \tag{13}$$

where MSE is the Mean Square Error calculation (RMSE squared), and BEF is the blocking non-reference quality index defined in Yim and Bovik, 2011. Higher values represent greater consistency with the original image, ideally infinite in the case of identical images, and generally fewer artefacts.

The Structural Similarity Index Measure was designed by Wang et al., 2004 focusing on structural convergence and is a combination of three different features, referred to as luminance, contrast, and structure:

$$SSIM(r, t) = [l(r, t)]^{\alpha} \bullet [c(r, t)]^{\beta} \bullet [s(r, t)]^{\gamma} \tag{14}$$

$$l(r, t) = \frac{2\mu_r \mu_t + C_1}{2\mu_r + \mu_t + C_1} \tag{15}$$

$$c(x, y) = \frac{2\sigma_r \sigma_t + C_2}{2\mu_r + \mu_t + C_2} \tag{16}$$

$$s(r, t) = \frac{\sigma_{xy} + C_3}{\sigma_r \sigma_t + C_3} \tag{17}$$

where α, β, and γ are exponents used to adjust the relative importance of the three components, otherwise equal to 1, and C1, C2, and C3 are small constants to avoid instabilities from division by 0, defined from the dynamic range L of the image as:

$$C_1 = (0.01L)^2, C_2 = (0.03L)^2, C_3 = 0.5\, C_2 \tag{18}$$

The local statistics (mean, standard deviation, and covariance) are computed within a moving 8x8 square window. The results can range from 0 to 1, with the upper margin referring to equal images.

In addition to the reduced-resolution comparison, the parameter is also used in this study to compare the quality of detail extracted from the original full-resolution PAN with a pseudo-panchromatic image derived from the sum of the three bands of the pansharpened MS.

5. Experimental results and considerations

In this section, we present the results obtained from two sets of experiments: in the first one, we compared MS and PAN source data, while in the second one, we compared the analysed CaSSIS images to the colour portion of HiRISE images at full resolution.

The RED of HiRISE was used at the acquisition resolution without subsampling, varying from about 25 to 50 cm/px, depending on the binning In this way, it was possible to test the algorithm's potential at its

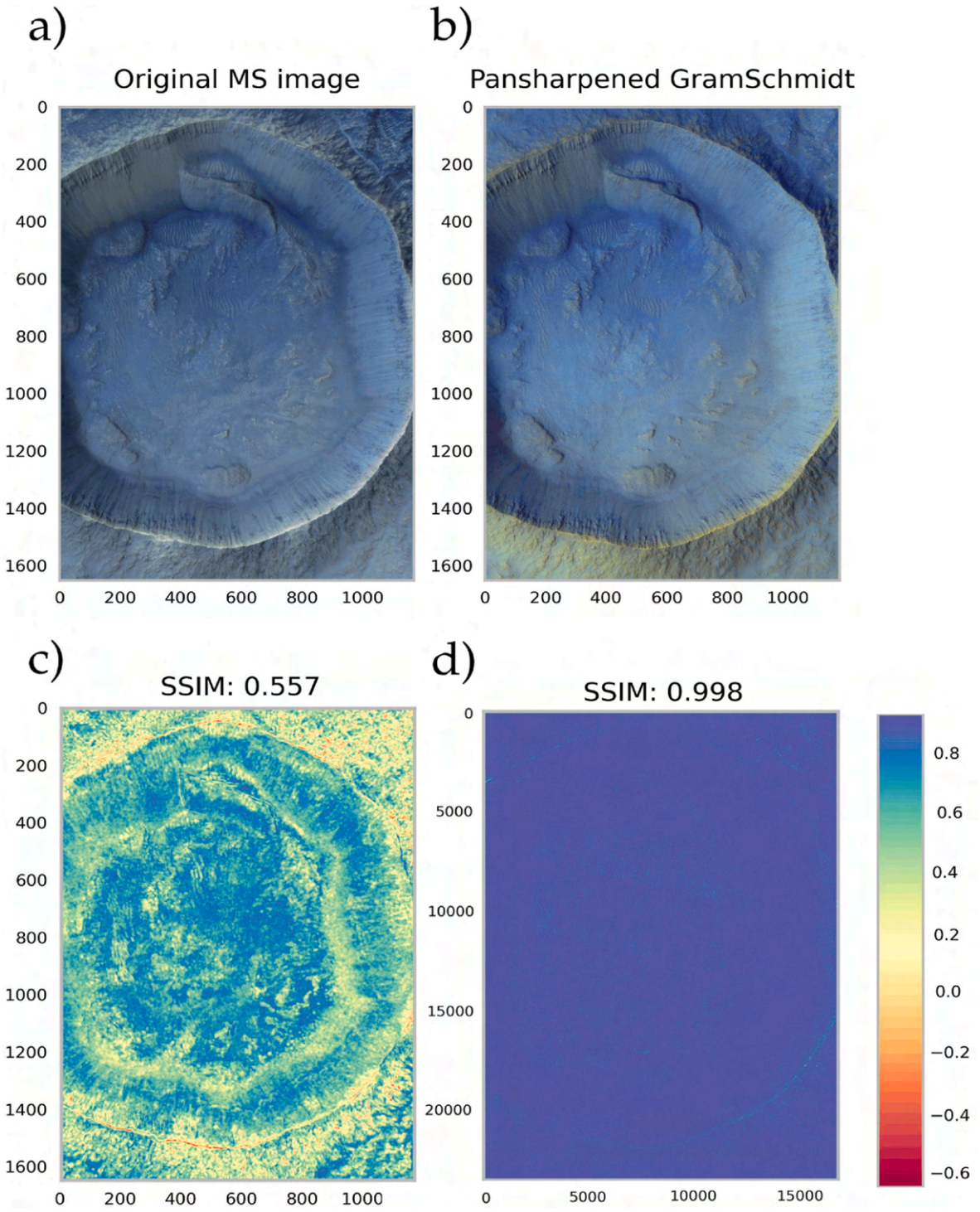

Fig. 7. Comparison of SSIM parameter maps for image (MY34_004795_342_1) pansharpened with the Gram-Schmidt algorithm. In the image: a) the original CaSSIS, b) the pansharpened image at RR (1170x1650 px), c) SSIM map between original and pansharpened version, d) SSIM map between reference PAN image (ESP_0123150_1635) and the summed intensity from the pansharpened CaSSIS at FR (16820x23720 px). The axes refer to the number of pixels, with (0,0) starting from the upper left corner. The image depicts Kenge Crater, a fresh equatorial impact crater in Tyrrhena Terra, studied for its exposed rock surface and distinct erosional shapes along the walls [Conway et al., 2018]. The crater also features a large landslide body in its northern part and recurring slope lineae.

highest resolution to date, thereby providing results at HiRISE's resolution. From the initial spatial resolution of 4.5 m/px, we increased the resolution between 9x and 18x with respect to the original CaSSIS images (Fig. 5).

The results include both visual analysis and evaluation of the indicators used. The following discusses and analyses various factors that may influence the quality of the final output.

5.1. Comparison with original MS and PAN

The experimental results on the entire dataset based on reduced- (4.5 m/px) and full- (0.25–0.5 m/px) resolution are assessed in terms of evaluation indexes. These are summarised in Table 3. The best three results for each index are marked in bold. The diverse nature of the approaches used leads to significantly different results, which are

Table 4
Averaged results of the method evaluation between colour HiRISE images and their simulation by pansharpening the CaSSIS data. For this analysis, a subset of clips from the test dataset limited to the portions that overlap the colour segment of the HiRISE image were used. For each algorithm, the three best results are highlighted in bold. The box plots below show the statistical distribution of the results. In the RMSE and ERGAS box graphs, Br and IHS are not shown because they are out of scale. In brackets the standard deviation, represented in the graphs as error bar.

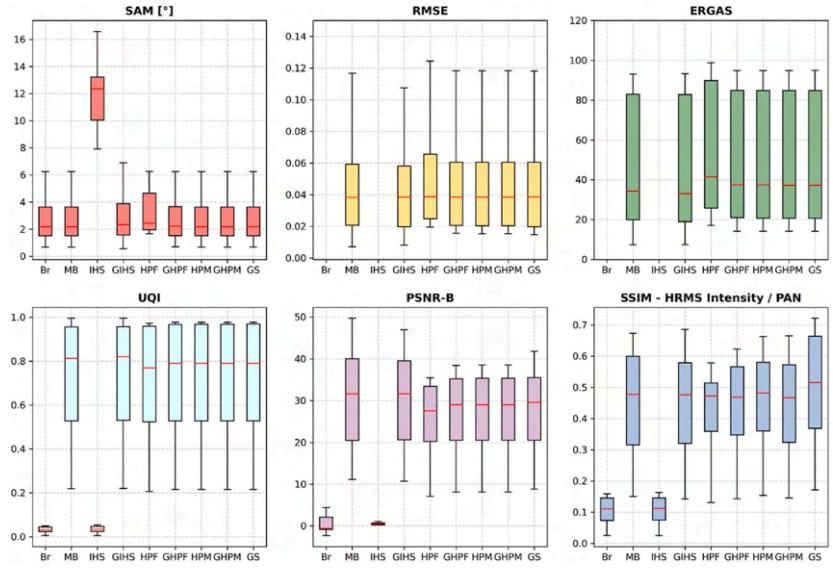

	SAM [°]	RMSE	ERGAS	UQI	PSNRB	SSIM
Brovey	**2.903 (2.028)**	0.989 (0.073)	1129.904 (716.204)	0.032 (0.016)	4.382 (14.854)	0.111 (0.046)
MMSE Brovey	**2.903 (2.028)**	**0.048 (0.038)**	**72.796 (93.042)**	**0.766 (0.29)**	**31.878 (11.157)**	**0.478 (0.15)**
IHS	12.352 (2.767)	0.962 (0.07)	1247.838 (738.999)	0.034 (0.018)	0.338 (0.699)	0.112 (0.047)
GIHS	3.067 (2.186)	**0.048 (0.038)**	**72.339 (93.241)**	**0.769 (0.29)**	**31.642 (10.716)**	0.477 (0.143)
HPF	3.546 (1.798)	0.054 (0.039)	80.929 (98.668)	0.753 (0.292)	27.541 (7.08)	0.445 (0.131)
GHPF	2.921 (2.017)	0.05 (0.038)	74.852 (94.879)	0.763 (0.292)	28.946 (8.073)	0.469 (0.143)
HPM	**2.903 (2.028)**	0.05 (0.038)	74.734 (94.892)	0.763 (0.292)	28.976 (8.103)	**0.482 (0.154)**
GHPM	**2.903 (2.028)**	0.05 (0.038)	74.704 (94.882)	0.763 (0.292)	28.985 (8.106)	0.466 (0.145)
Gram-Schmidt	2.919 (2.022)	**0.049 (0.039)**	**74.581 (94.902)**	**0.764 (0.292)**	**29.578 (8.816)**	**0.522 (0.172)**

reflected in the indexes.

The traditional Brovey and IHS implementations are not based on histogram normalisation or equalisation and thus tend to show the worst performance in terms of spectral deformation. In contrast, these methods perform well in structural implementation, showing high SSIM values compared to the HiRISE RED image.

Recent variants of these methods tested here, like MMSE Brovey and GIHS, show a significant increase in output performances. Indeed, MMSE Brovey's approach shows better results than GIHS in preserving the spectral shape. However, it is characterised by more variability in index values. From the visual analysis, a general over-saturation of colours is observed in the case of GIHS and, although less pronounced, in MMSE. These properties and the marked increase in structural properties make GIHS and MMSE Brovey particularly appropriate for use in scenarios that benefit from well-defined boundaries. For example, in geological mapping, such methods can facilitate the distinction of limits between different colours and, thus, between different geological units or in the discretisation of geomorphological features.

On the other hand, the HPM, GHPF and GHPM methods stand out for their high spectral fidelity, achieving near-ideal results in spectral indexes. This precision and accuracy make them the most appropriate for numerical analysis purposes, such as spectra observations and end-member extraction scenarios. However, it is essential to note that these algorithms do not achieve the same sharpening effect as the other techniques, often exhibiting generally blurred details in visual analysis and lower SSIM values compared to the HiRISE RED image. This effect is further evidenced by comparing the SSIM values of the HiRISE RED and original MS images, respectively in blue and red in the graph in Fig. 6. Among these, the GHPF method shows generally higher contrasts, allowing to highlight more details of the starting PAN but also possible noise. Such graininess is not perceived in GHPM, whose smooth effect makes it particularly useful in scenarios where the PAN exhibits low SNR that would otherwise affect the result.

Overall, the Gram-Schmidt algorithm gives the best compromise between preserving spectral properties and sharpening. It shows low spectral error rates, good signal-to-noise ratio, and excellent SSIM in both RR and FR analyses (Fig. 7). The minimal spectral distortion indicates a colour rendition consistent with the original, and the nature of orthogonalisation and the use of spline resampling during oversampling, has a mitigating effect on any bad pixels in the source MS, unlike other methods. This versatility makes it the most reasonable method for most usage scenarios, especially for studies that combine different analysis techniques. In addition, the mitigation of the error component in the source data makes it particularly effective for use with MS characterised by low SNR.

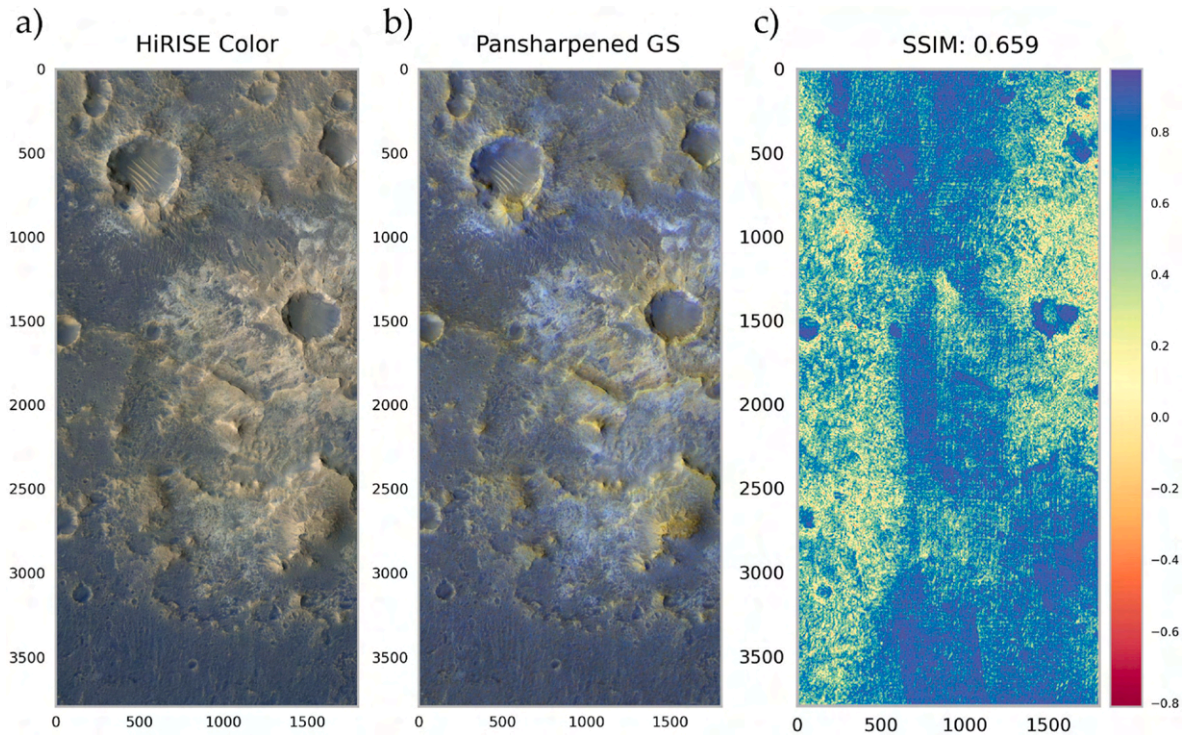

Fig. 8. The SSIM colour map (c) derived from the comparison between the HiRISE Colour PSP_010394_2025 (a) and the CaSSIS image MY34_004209_158_0 pansharpened with GS method (b) highlights an artefacts oblique to the image frame. Given the position and linear variation, this was interpreted as the result of differences between HiRISE channels that are not reflected in (b). The presence of artefacts between the two instruments may influence the evaluation indexes, making comparison more difficult. The axes refer to the number of pixels, with (0,0) starting from the upper left corner.

5.2. Comparison with HiRISE colour images

The colour portion of the HiRISE images provides a ground truth to which we can compare the results.

Although it covers a similar spectral range of HiRISE, CaSSIS camera has the >800 m NIR range observed in two bands, identified as 'Red' (785–885 nm) and 'Near-Infrared' (880–1000 nm) (cf. also Table 1). The division between RED and NIR in CaSSIS allows for a significant increase in mineralogical diagnostics (Tornabene et al., 2018).

To simulate the unique IR band of the HiRISE data, the two bands of CaSSIS are averaged into a single band. Furthermore, since in the HiRISE, the I/F signal between RED and IR covers a similar range of values (Delamere et al., 2010), the generated IR band in CaSSIS is also mean-matched with the HiRISE RED band. Due to the intrinsic properties of the observed surface, the BG band signal for both instruments is generally lower than for the others. However, a discrepancy is observed whereby this is, on average, 30% lower for HiRISE than the average of the other two bands, compared to 45% lower for HiRISE. This is probably caused by the narrower spectral range sampled by the BG filter of CaSSIS compared to HiRISE (425–560 vs. 400–580, respectively and implies a slight difference in the slope of the spectrum, which has a higher inclination in the case of CaSSIS.

Table 4 shows the evaluation results between colour HiRISE data and their simulation by pansharpening.

Despite the simulation of the IR band, the diverse nature of the instruments, misalignments, and the presence of different sensor-related artefacts (Fig. 8) lead to a certain degree of differences between images and in the ranges of I/F units. This is reflected in a general deterioration of the performance indicators, which must be considered more for their correlative importance than for the absolute values.

Contrary to what was observed in RR analyses, HP-based methods show generally lower indicators than MMSE Brovey (MB), GIHS, and Gram-Schmidt (GM) methods. This is probably related to the lower sharpening capacity of the methods, where blurred details are not mitigated in the FR analyses as in the RR ones (Scarpa and Ciotola, 2022). The MMSE Brovey, GIHS, and Gram-Schmidt methods show overall robust performance with very slight changes in colour ranges (Fig. 9). At the same colour scale, the former tends to preserve more of the difference in values between PAN and IR (Fig. 9f). In contrast, the others tend to flatten out, resulting in a subtle yellow colouration (Fig. 9d and e).

As obtained for previous analyses, Brovey and IHS implementations have the most significant alteration of spectral properties, which is generally reflected in all the indicators used.

5.3. Considerations on the influence of band combinations and lighting conditions

Table 5 and Fig. 10 display the results according to the band combinations used in the source images, RED/PAN/BG and NIR/PAN/BG. Although the indicators show similarly reliable results in both cases, the analysis highlights slightly better values for the first combination (RPB) in several spectral and structural indicators. These values could be due to the almost complete spectral coverage of the RED band of CaSSIS by the RED of HiRISE instead of the NIR, which falls outside. Despite this, the differences are less pronounced than expected and inconsistent across all the methods.

Contrary to expectations, even different illumination conditions between the MS image and the PAN show no detrimental degradation in the final result.

Table 6 and Fig. 11 report the test results divided into three different ranges of Solar Azimuth differences: less than 30°, between 50° and 80°, and above 120°. The Solar Incidence differences along the dataset are smaller, related to the limits of the acquisition geometry, and consistently below 30°.

Differing from the spectral indicators, which show no significant change, structural indexes generally show slightly better results under similar lighting conditions, albeit not always evident. This is mainly

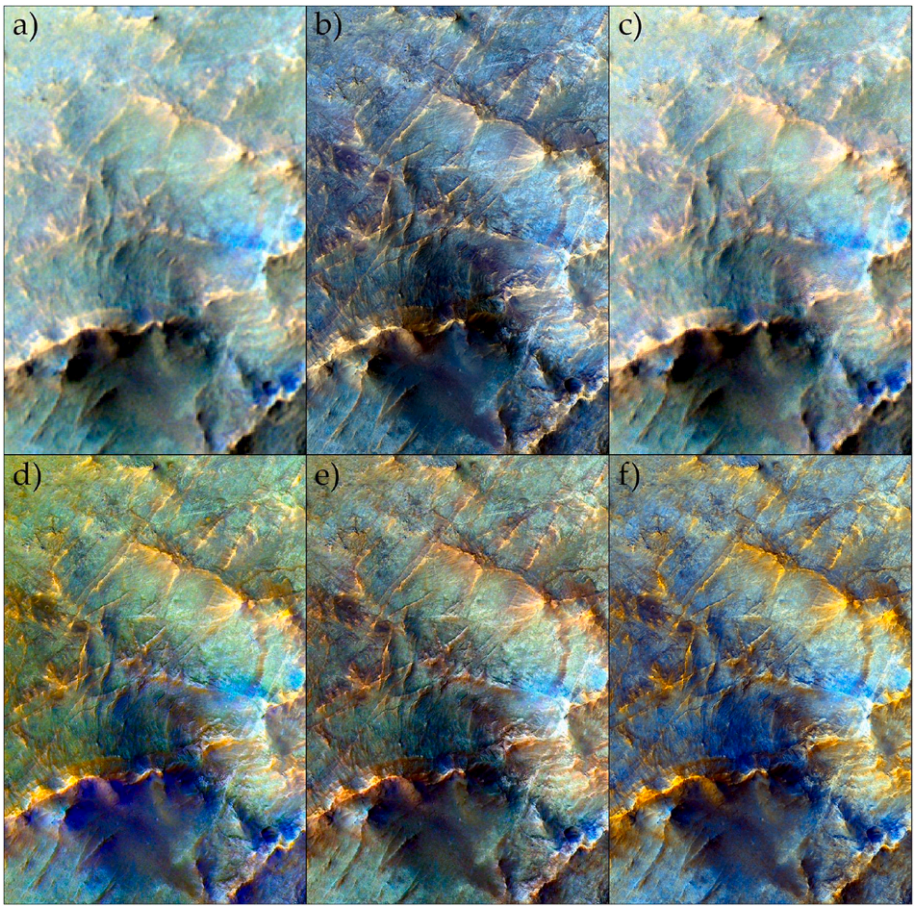

Fig. 9. Visual comparison of different algorithms results compared to the simulated HiRISE-band CaSSIS image (MY34_002260_337_0) (a) and to the aligned HiRISE colour image (ESP_012989_1585) (b). The methods shown are c) GHPM, d) GIHS, e) MMSE Brovey, and f) Gram-Schmidt. The contrast stretching is set at 2% to emphasise visual details. By visual analysis, GIHS and MMSE Brovey show the best increase in detail compared to HiRISE, but slightly oversaturated colours compared to the colour fidelity of GHPM and GS. The image depicts various ridges and erosional morphologies on the northern edge of the Hellas Basin. The region is being studied for the presence of olivine-rich units and feldspathic lithologies possibly the result of uplift of pre-Noachian (>4.1 Ga) crustal blocks due to Hellas impact or the subsequent volcanic activity Phillips et al., 2022.

Table 5
Average results of method evaluation divided by band combination, left RED/PAN/BG and right NIR/PAN/BG. The best results between the two are highlighted in bold.

	SAM [°]	RMSE	ERGAS	UQI	PSNRB	SSIM MS (RR)	SSIM PAN (FR)
Brovey	0.017 - **0.007**	0.91 - **0.868**	80.484 - **55.233**	0.07 - **0.104**	18.224 - **30.114**	0.136 - 0.133	**1**–**1**
MMSE Brovey	**0.008**–**0.008**	**0.008** - 0.018	**0.574** - 1.217	**0.996** - 0.972	**43.036**–36.952	0.617 - 0.448	**0.993** - 0.63
IHS	13.118 - **11.588**	0.878 - **0.842**	91.293 - **61.153**	0.072 - **0.105**	5.959 - **14.64**	0.134 - 0.134	**1**–**1**
GIHS	**0.71** - 0.907	**0.007** - 0.014	**0.625** - 0.77	**0.995** - 0.985	**45.637** - 40.495	0.67 - 0.594	**1**–0.991
HPF	2.862 - **2.749**	**0.02** - 0.031	2.619 - **2.196**	**0.966**–**0.967**	**35.0**–30.811	0.478 - 0.426	**0.749** - 0.601
GHPF	**0.165** - 0.289	**0.002** - 0.004	**0.185** - 0.268	**1**–**0.999**	**54.672** - 53.135	0.703 - 0.646	**0.951** - 0.911
HPM	**0.008**–**0.008**	**0.002** - 0.005	**0.214** - 0.268	**1**–**0.999**	**50.884** - 49.032	0.671 - 0.651	**0.955** - 0.883
GHPM	**0.008**–**0.008**	**0.001** - 0.002	**0.055** - 0.079	**1**–**1**	**61.85**–**61.01**	0.918 - 0.887	**0.925** - 0.921
Gram-Schmidt	**0.344** - 0.449	**0.004** - 0.007	**0.287** - 0.332	**0.999**–**0.998**	**46.921** - 42.169	0.609 - 0.583	**0.997** - 0.999

attributable to the fact that, apart from HP-based methods that exclude the shadows component, all the methods tested have a tendency to attribute the light conditions of the PAN to the final result (Fig. 12). This is particularly evident in PSNR-B, the indicator most influenced by local distortions, which in this case are represented by the different shaded areas between original and processed. In these cases, methods that maintain the initial conditions (HP-based) show significantly better results compared to others. In addition, shaded areas in the original MS image are more prone to being over-coloured with methods that highlight colours, such as GIHS and Gram-Schmidt.

Although this does not affect most scenarios, studies requiring the preservation of original illumination conditions should use methods that

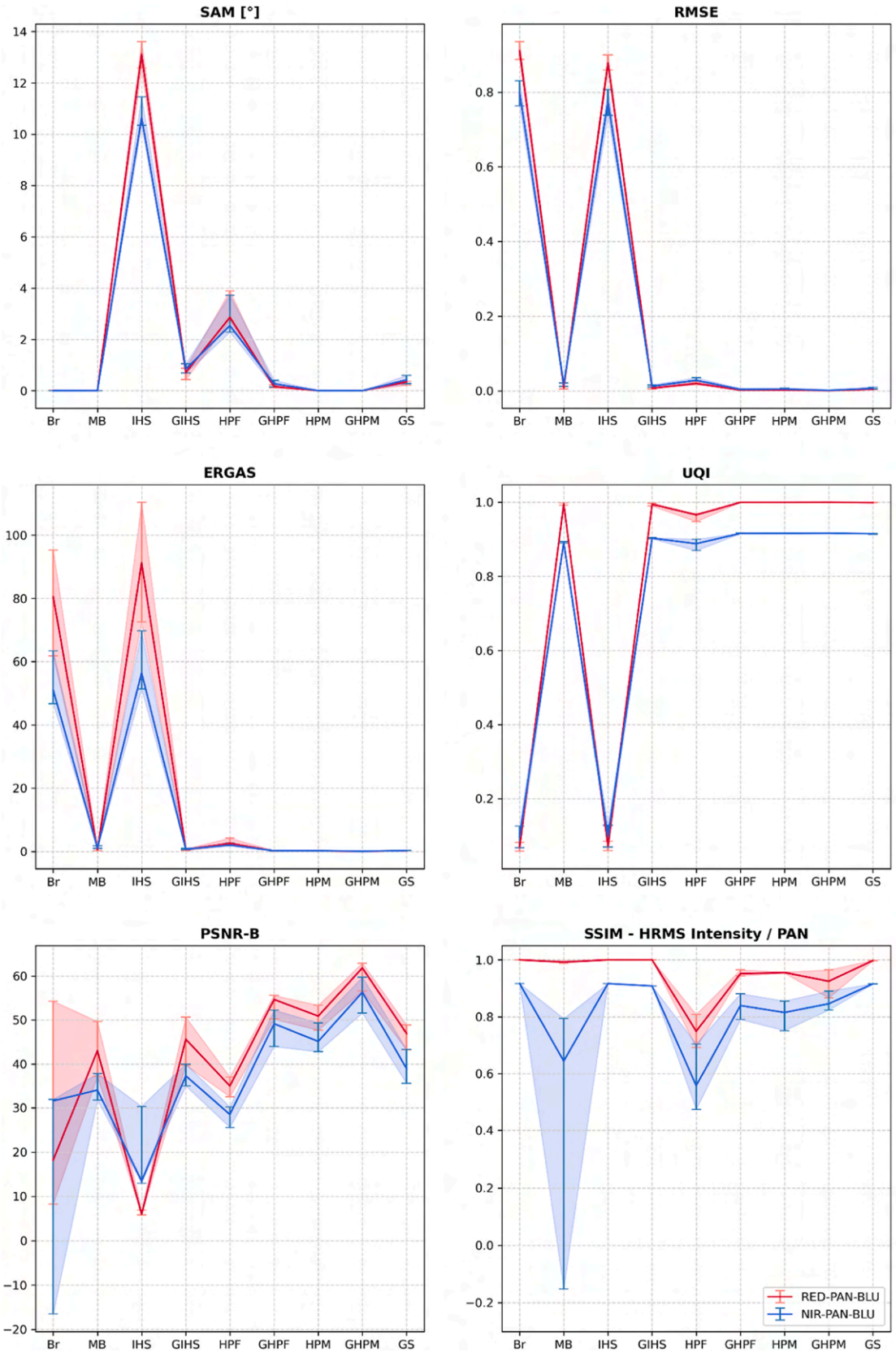

Fig. 10. Trend of test results divided by band combination: in red RED/PAN/BG and in blue NIR/PAN/BG. For the first three parameters (SAM, RMSE, ERGAS) lower is better, on the contrary for the remaining ones. The portion highlighted by the error bars represents the top of the Gaussian distribution between first and third quartiles.

Table 6
Average results of evaluations, divided by different ranges of solar azimuth differences: from left to right, similar (<30°), midpoint (50–80°), and opposite conditions (>120°). The best results of the three are given in bold.

	SAM [°]	RMSE	ERGAS	UQI	PSNRB	SSIM MS (RR)*	SSIM PAN (FR)**
Brovey	**0.032** - 0.007 - 0.007	0.881 - **0.861** - 0.88	**45.648** - **45.583** - 91.987	0.091 - **0.118** - 0.082	23.355 - 28.348 - **35.525**	0.202 - 0.122 - 0.1	**1–1** - **1**
MMSE Brovey	**0.008–0.008–0.008**	**0.029** - 0.007 - 0.017	1.345 - **0.376** - 2.143	0.958 - **0.998** - 0.963	32.526 - **42.259** - 34.316	0.635 - 0.357 - 0.492	**0.973** - 0.504 - 0.629
IHS	12.323 - **11.72** - 11.797	0.851 - **0.834** - 0.854	52.766 - **51.45** - 101.101	0.093 - **0.12** - 0.084	**13.433** - 11.215 - **13.432**	0.198 - 0.122 - 0.101	**1–1** - **1**
GIHS	1.7 - **0.488** - 0.864	0.024 - **0.007** - 0.01	1.342 - **0.434** - 0.915	0.962 - **0.998** - 0.993	35.845 - **43.898** - 40.199	0.714 - 0.545 - 0.602	**0.975** - **1** - **1**
HPF	**1.06** - 2.212 - 4.218	**0.018** - 0.036 - 0.028	**0.947** - 1.899 - 3.421	**0.992** - 0.975 - 0.947	35.711 - 29.72 - 31.243	0.612 - 0.344 - 0.414	**0.665** - 0.644 - 0.546
GHPF	0.223 - **0.205** - 0.424	**0.003** - 0.004 - 0.006	0.2 - **0.192** - 0.454	**1–1** - **0.999**	**63.457** - 50.122 - 45.674	0.738 - 0.619 - 0.62	0.849 - **0.972** - 0.915
HPM	**0.008–0.008–0.007**	**0.004** - 0.007 - **0.004**	**0.165** - 0.299 - 0.278	**1–0.999–1**	**60.854** - 42.776 - 47.413	0.843 - 0.506 - 0.726	0.762 - **0.982** - 0.915
GHPM	**0.008–0.008–0.007**	**0.001** - **0.001** - 0.002	0.06 - 0.055 - **0.134**	**1–1** - **1**	**71.446** - 57.745 - 53.197	0.904 - 0.896 - 0.868	**0.955** - 0.925 - 0.888
Gram-Schmidt	0.503 - **0.371** - 0.555	0.007 - **0.006** - 0.009	0.364 - **0.31** - 0.485	**0.998** - **0.999–0.998**	40.772 - **43.891** - 40.657	0.685 - 0.493 - 0.644	**0.999** - **0.999–0.998**

exclude shadows, such as GHPF and GHPM, or choose images with similar lighting conditions.

Another option might include a preprocessing step that includes photometric correction of the PAN, f that would favour a general mitigation of the scene's overall light conditions.

5.4. Processing times

Fig. 13 shows the average processing times and peak memory usage for processing the test dataset, obtained through an Intel Xeon w7-2475X processor (20 Core) workstation.

As shown in Fig.13, CS pansharpening methods confirm their computational efficiency. None of the tested implementations stands out due to excessive computational burden, with processing times spanning from 2 to about 10 min in the case of the larger images. GS stands out for the lower processing times among the tested methods, probably due to the NumPy optimization for vectors, making vectorisation of the images an essential part of the process. The use of resources such as volatile memory is equally quite similar among the methods and directly related to the size of the images, with a peak for the HPM and GHPM methods, which simultaneously store the bands and their estimated modulation coefficients.

It is important to note that none of the tools developed so far have been designed with a focus on optimising resources, so further development could potentially lead to significant reductions in computational load and times. For example, none of the developed implementations have comprehended a parallelisation of processes so far. Simultaneous processes handling small tiles of the processed images could be implemented for several of the methods tested and lead to substantial cuts in processing time.

5.5. CaSSIS/CRISM applications

In the test results considered in this work, we derive a general minimisation of the spectral shape distortion traditionally considered the downside of pansharpening. This information is crucial for spectral analyses on multi- and hyperspectral data. Some of the CS methods tested, such as GS, are adapted or adaptable to handling the number of bands typical of hyperspectral data (Laben and Brower, 2000; Loncan et al., 2015).

The CRISM instrument on board the MRO mission represents the highest spatial resolution hyperspectral camera ever sent to Mars, an essential resource for studying the planet's mineralogy (Murchie et al., 2007). CRISM allows hyperspectral resolution observations, sampling the spectral range between 360 and 3920 nm at 6.55 nm/channel and at a medium-high spatial resolution up to 16 m/px.

During the experiments, some tests were conducted on the combined use of CRISM and CaSSIS, using the latter no longer for its multispectral qualities but as a higher-resolution PAN. In this way, it was possible to increase the resolution of the 3-band CRISM images by factors of 4x to 8x, depending on the source products (Fig. 14).

Similar results were previously observed by Tornabene et al. (2018) for the simulation of the CaSSIS data. In addition to the implementation of the resolution, visual analysis of the results highlighted an effect of general noise mitigation across the image. However, this effect and the deformation of the spectral properties for a larger number of bands, typical of hyperspectral, require further targeted investigations, which were not conducted in the course of this study. Such developments could potentially improve the mineralogical characterisation analyses conducted on Mars today.

6. Conclusions

In this paper, several CS pansharpening methods were applied in the context of Mars observations by improving the MS CaSSIS data up to 18x in spatial resolution using HiRISE, reaching up to 0.25 m/px. Increasing resolution is a significant advantage that can facilitate surface studies, geological interpretation and mapping, and support spectral analysis and endmember extraction.

A structural and spectral evaluation was performed, highlighting the strengths and weaknesses of the tested radiometric transformation algorithms. Evaluations were conducted by comparing the source data at RR with the central HiRISE colour portion at FR.

In general, almost all tested algorithms performed well, and the preference of one method over another must be weighed according to a given application. The MMSE Brovey and GIHS methods are the most suitable for pure resolution enhancement but exhibit a slight but non-negligible spectral distortion component. In contrast, the HPM, GHPF, and GHPM methods allow near-ideal preservation of spectral properties in tests at the expense of a less defined enhancement of image structure.

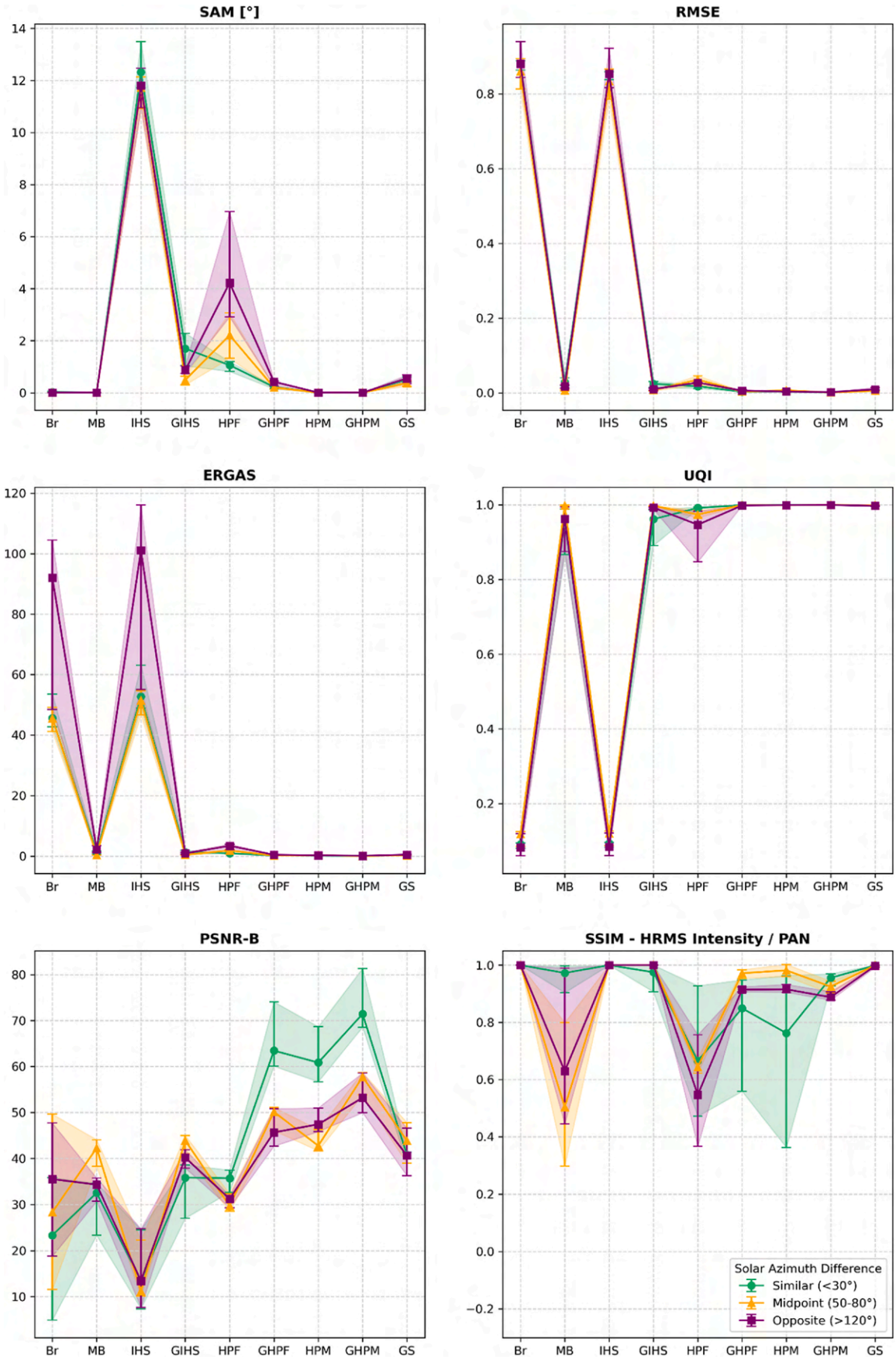

Fig. 11. Subset of test results by solar azimuth difference between MS and PAN: <30° in green, 50–80° in gold, and >120° in red. The error, subtended by the coloured area, is here indicated by the interval between the first and third quartile.

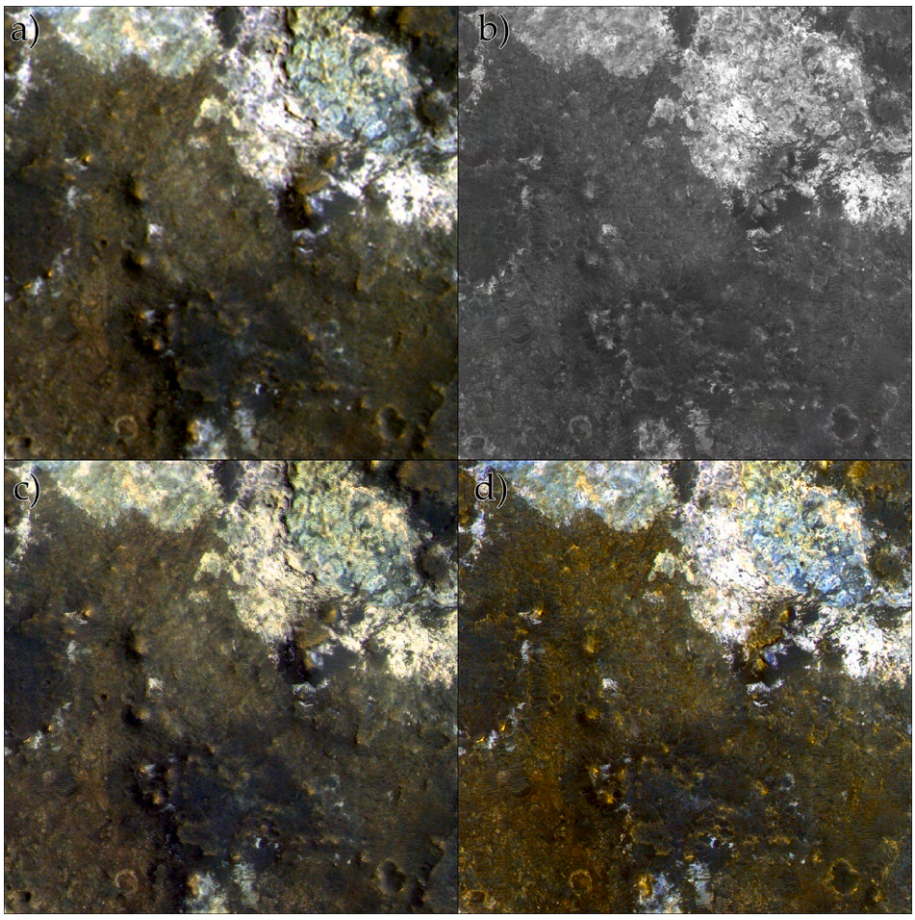

Fig. 12. Comparison of the results under different light conditions between (a) MS (CaSSIS image (MY36_016518_157_0) acquired with N73° solar azimuth) and (b) PAN (the RED band from HiRISE image ESP_051153_2025) acquired with N244°) of origin: (c) GHPF and (d) Gram-Schmidt. The area, located in the plateau south of Mawrth Vallis, is interested by bright hydrous minerals and clays-rich deposits typical of the northwestern Arabia Terra Loizeau et al., 2007.

The Gram-Schimdt method generally provides the best compromise between the other methods tested with positive indexes in all scenarios considered.

In addition, the effects of different combinations of bands and lighting conditions were analysed. Tests have shown that the algorithms tend to work well regardless of the nature of the input bands, although slightly better performance is reported in the case of the RED-PAN-BLU over the NIR-PAN-BLU band combination. Similarly, opposite illumination conditions between MS and PAN do not affect the performance of the tested algorithms. For the algorithms under analysis, the illumination conditions of the resulting data are inherited from PAN, except for algorithms based on high-pass (HP) filters where the conditions remain consistent with the original.

The key factors influencing the output appear to be the quality of the source images and their alignment. Future developments include evaluating further methods and applications to other instruments and planetary bodies.

7. Future work

The ever-increasing number of hyperspectral sensors has further driven the development of pansharpening methods that allow the resolution to be implemented without affecting the spectrum properties. In addition to the methods tested in the study, other CS, MRA, and ML methods were created specifically for this purpose (Wei et al., 2015; He et al., 2019; Xie et al., 2021). Future studies will involve testing different techniques suited to the hyperspectral nature of the data and validation in the context of planetary science studies.

Beyond Mars, the combined use of CaSSIS and HiRISE represents a relatively large resolution ratio that opens the door to many further applications, and the methods tested represent some of the most easily adaptable pansharpening methods for different instrument types.

Among them, the BepiColombo mission to Mercury will carry into orbit the SIMBIO-SYS (Spectrometers and Imagers for MPO BepiColombo Integrated Observatory SYstem) instrument suite consisting of three independent camera systems (Flamini et al., 2010; Cremonese et al., 2020): the VIHI (Visible and Infrared Hyperspectral Imager) with hyperspectral capabilities, the STC (Stereo Channel) double wide-angle camera for colour and stereo imaging and the high-resolution HRIC (High resolution Imaging Camera) camera (Fig. 15). In addition to its stereo imaging objectives for three-dimensional surface reconstruction, STC bridges the resolution gap between the other two instruments. In the field of pansharpening, STC can be used both as PAN for VIHI enhancement and as MS for HRIC data.

The first version of the developed suite can be found at: http://hdl.handle.net/20.500.12386/35184 - Code name 'Project PANCO (PANsharpening and COregistration suite)'. CaSSIS data used in this work are available in the European Space Agency's Planetary Science Archive (PSA): https://archives.esac.esa.int/psa/and at the official archive of the University of Bern: https://observations.cassis.unibe.ch/. HiRISE data used are available in the Planetary Data System (PDS): https://www.uahirise.org/.

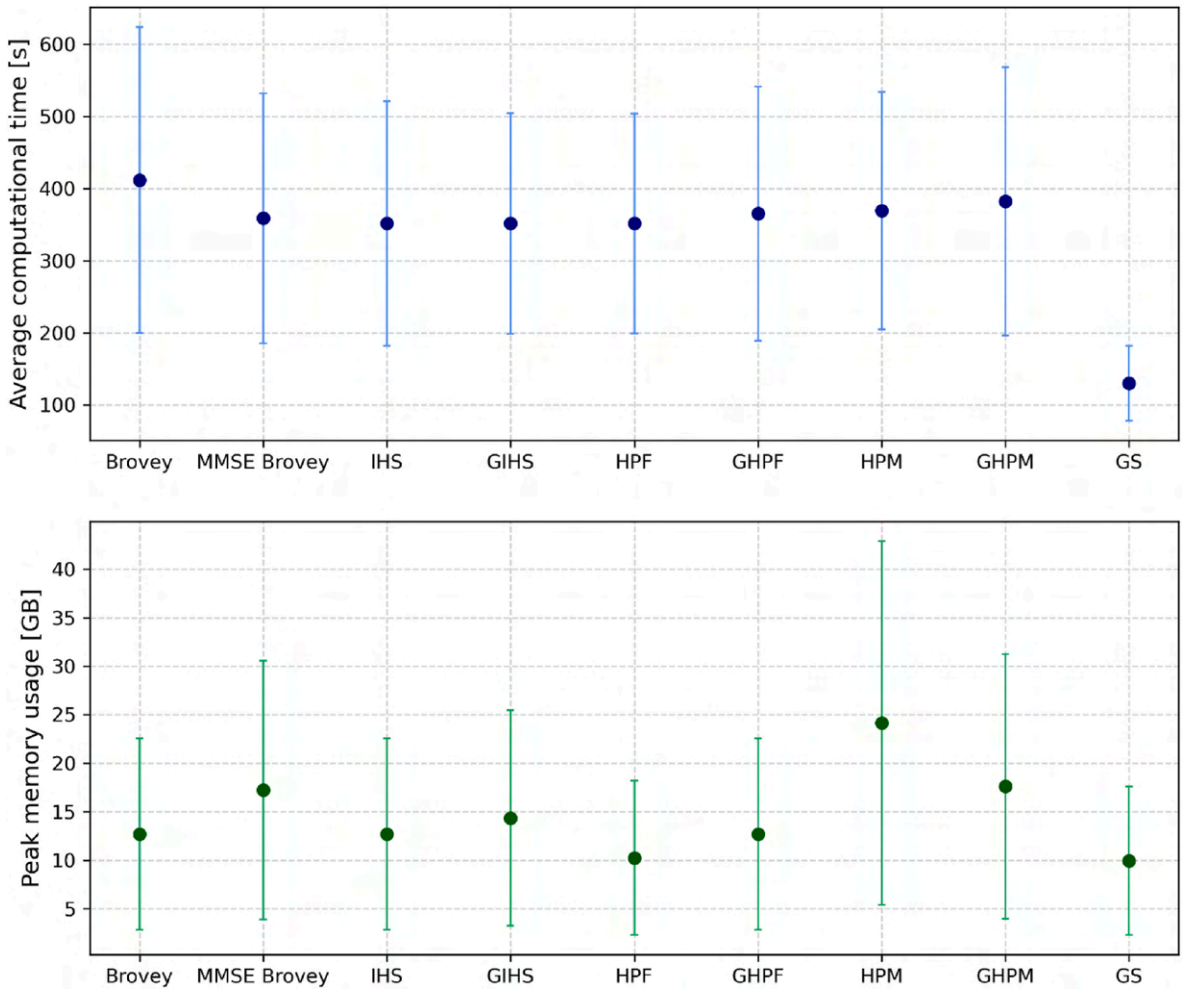

Fig. 13. Computational resource utilization for the tools tested with error bars indicating the measured standard deviation. The variability within the same methods is a function of the size of the processed tiles and the scaling factor between source MS and PAN.

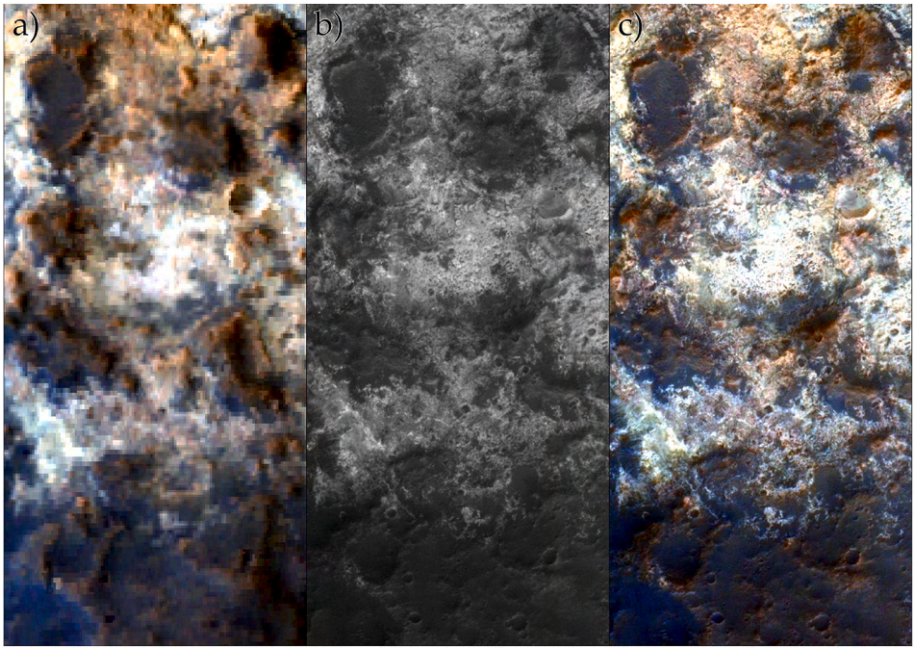

Fig. 14. Application of pansharpening to CRISM/CaSSIS implementation: a) original CRISM Enhanced Visible RGB (R600, R530, R440) FRT00003BFB_07_IF166J_MTR3, b) CaSSIS MY35_012994_023_0 image and c) Gram-Schmidt pansharpened result. The area portrayed in the image, within Mawrth Vallis, is of great interest due to the presence of carbonates, in addition to Al and Fe/Mg clays, with possible implications for the reconstruction of climatic palaeoenvironments of Mars and, ultimately, its geological evolution Bultel et al., 2019.

	Resolution [m/px]	N.Bands	Spectral Range [nm]
VIHI	120 – 480	256	408.03 – 2006.34
STC	50 – 120	6	400 – 940
HRIC	5 – 12	4	400 – 900

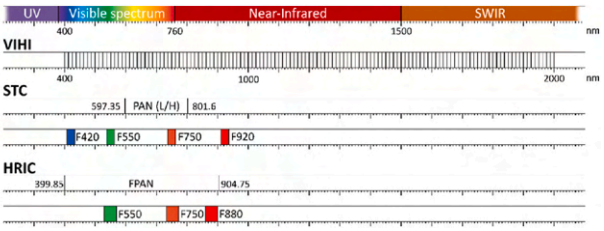

Fig. 15. Spatial and spectral properties of the SIMBIO-SYS cameras [Cremonese et al., 2020] and graphical visualisation. The use of pansharpening offers various possibilities for integration between instruments, allowing different bands and resolutions to be combined.

CRediT authorship contribution statement

A. Tullo: Writing – review & editing, Writing – original draft, Visualization, Validation, Software, Methodology, Investigation, Funding acquisition, Formal analysis, Data curation, Conceptualization. **C. Re:** Writing – review & editing, Project administration, Investigation. **G. Cremonese:** Writing – review & editing, Supervision, Funding acquisition. **E. Martellato:** Writing – review & editing, Visualization, Validation. **R. La Grassa:** Writing – review & editing. **N. Thomas:** Writing – review & editing, Supervision.

Declaration of competing interest

The authors declare that they have no known competing financial interests or personal relationships that could have appeared to influence the work reported in this paper.

Acknowledgement

The study has been supported by the Italian Space Agency (ASI-INAF agreement no. 2020-17-HH.0) and INAF (INAF MiniGrant "Combined implementation of CaSSIS and HiRISE data through pansharpening experiments" - CUP C93C23008430001). Thanks to the CaSSIS Team for the precious advice and feedback.

Acronyms and abbreviations

BG	Blue-Green
BLU	Blue
Br	Brovey
CCD	Charge-coupled device
CMOS	Complementary metal–oxide–semiconductor
CRISM	Compact Reconnaissance Imaging Spectrometer for Mars
CS	Component Substitution
CaSSIS	Colour and Stereo Surface Imaging System
ERGAS	Erreur Relative Globale Adimensionnelle de Synthèse
FR	Full resolution
(G)HPF	(Generalized) High-Pass Filtering
(G)HPM	(Generalized) High-Pass Modulation
GS	Gram-Schmidt
(G)IHS	(Generalized) Intensity, Hue and Saturation Transformation
HiRISE	High Resolution Imaging Science Experiment
IR	Infrared
ML	Machine/Deep Learning
MMSE	Minimum mean square error
MOC	Mars Orbital Camera
MRA	Partial Replacement Adaptive Component Substitution
MRO	NASA Mars Reconnaissance Orbiter
MS	Multispectral
NIR	Near-Infrared
PAN	Panchromatic
PSNR-B	Peak Signal-to-Noise Ratio with blocking effect
RMSE	Root Mean Square Error
RR	Reduced resolution
SAM	Spectral Angle Mapper
SIFT	Scale-invariant feature transform
SNR	Signal-to-Noise ratio
SSIM	Structural Similarity Index Measure
TGO	ESA ExoMars Trace Gas Orbiter
UQI	Universal Quality Index
VO	Variational Optimization-Based

References

Aiazzi, B., Alparone, L., Baronti, S., Garzelli, A., Selva, M., 2012. Advantages of Laplacian pyramids over « "à trous" » wavelet transforms for pansharpening of multispectral images. Image and Signal Processing for Remote Sensing XVIII 8537, 12–21. https://doi.org/10.1117/12.976298.

Aiazzi, B., Baronti, S., Selva, M., 2007. Improving component substitution Pansharpening through multivariate regression of MS +Pan data. IEEE Trans. Geosci. Rem. Sens. 45 (10), 3230–3239. https://doi.org/10.1109/TGRS.2007.901007.

Alcaras, E., Parente, C., Vallario, A., 2021. Automation of Pan-Sharpening methods for pléiades images using GIS basic functions. Rem. Sens. 13 (8), 1550. https://doi.org/10.3390/rs13081550.

Alparone, L., Aiazzi, B., Baronti, S., Garzelli, A., 2015. Remote Sensing Image Fusion. CRC Press.

Alparone, L., Wald, L., Chanussot, J., Thomas, C., Gamba, P., Bruce, L.M., 2007. Comparison of pansharpening algorithms: outcome of the 2006 GRS-S data-fusion contest. IEEE Trans. Geosci. Rem. Sens. 45 (10), 3012–3021. https://doi.org/10.1109/TGRS.2007.904923.

Bovolo, F., Bruzzone, L., Capobianco, L., Garzelli, A., Marchesi, S., Nencini, F., 2010. Analysis of the effects of pansharpening in change detection on VHR images. Geosci. Rem. Sens. Lett. IEEE 7 (1), 53–57. https://doi.org/10.1109/LGRS.2009.2029248.

Bradski, G., 2000. The OpenCV Library. Dr. Dobb's Journal of Software Tools.

Bruzzone, L., Carlin, L., Alparone, L., Baronti, S., Garzelli, A., Nencini, F., 2006. Can multiresolution fusion techniques improve classification accuracy? Proc. SPIE. https://doi.org/10.1117/12.691208.

Bultel, B., Viennet, J.-C., Poulet, F., Carter, J., Werner, S.C., 2019. Detection of carbonates in martian weathering profiles. J. Geophys. Res.: Planets 124 (4), 989–1007. https://doi.org/10.1029/2018JE005845.

Carper, W., Lillesand, T., Kiefer, R., 1990. The use of intensity-hue-saturation transformations for merging SPOT panchromatic and multispectral image data. Photogramm. Eng. Rem. Sens. 56 (4), 459–467.

Castillejo-González, I.L., 2018. Mapping of olive trees using pansharpened QuickBird images: an evaluation of pixel- and object-based analyses. Agronomy 8 (12), 12. https://doi.org/10.3390/agronomy8120288.

Chavez, P., Sides, S.C., Anderson, J.A., 1991. Comparison of three different methods to merge multiresolution and multispectral data- Landsat TM and SPOT panchromatic. Photogramm. Eng. Rem. Sens. 57 (3), 295–303.

Cheng, P., Chaapel, C., 2010. Pan-sharpening and geometric correction: worldview-2 satellite. Geoinformatics 13 (4), 30.

Ciotola, M., Vitale, S., Mazza, A., Poggi, G., Scarpa, G., 2022. Pansharpening by convolutional neural networks in the full resolution framework. IEEE Trans. Geosci. Rem. Sens. 60, 1–17. https://doi.org/10.1109/tgrs.2022.3163887.

Conway, S.J., Butcher, F.E.G., De Haas, T., Deijns, A.A.J., Grindrod, P.M., Davis, J.M., 2018. Glacial and gully erosion on Mars: a terrestrial perspective. Geomorphology 318, 26–57. https://doi.org/10.1016/j.geomorph.2018.05.019.

Cremonese, G., Capaccioni, F., Capria, M.T., Doressoundiram, A., Palumbo, P., Vincendon, M., Massironi, M., Debei, S., Zusi, M., Altieri, F., Amoroso, M., Aroldi, G., Baroni, M., Barucci, A., Bellucci, G., Benkhoff, J., Besse, S., Bettanini, C., Blecka, M., et al., 2020. SIMBIO-SYS: scientific cameras and spectrometer for the BepiColombo mission. Space Sci. Rev. 216 (5), 75. https://doi.org/10.1007/s11214-020-00704-8.

Delamere, W.A., Tornabene, L.L., McEwen, A.S., Becker, K., Bergstrom, J.W., Bridges, N. T., Eliason, E.M., Gallagher, D., Herkenhoff, K.E., Keszthelyi, L., Mattson, S., McArthur, G.K., Mellon, M.T., Milazzo, M., Russell, P.S., Thomas, N., 2010. Color imaging of Mars by the high resolution imaging science experiment (HiRISE). Icarus 205 (1), 38–52. https://doi.org/10.1016/j.icarus.2009.03.012.

Deng, L., Vivone, G., Paoletti, M.E., Scarpa, G., He, J., Zhang, Y., Chanussot, J., Plaza, A., 2022. Machine Learning in Pansharpening: a benchmark, from shallow to deep networks. IEEE Geosci. Remote Sensing Magazine 10 (3), 279–315. https://doi.org/10.1109/MGRS.2022.3187652.

Du, Q., Younan, N., King, R.L., Shah, V., 2007. On the performance evaluation of pan-sharpening techniques. Geosci. Rem. Sens. Lett. IEEE 4 (4), 518–522. https://doi.org/10.1109/lgrs.2007.896328.

Flamini, E., Capaccioni, F., Colangeli, L., Cremonese, G., Doressoundiram, A., Josset, J.L., Langevin, Y., Debei, S., Capria, M.T., De Sanctis, M.C., Marinangeli, L., Massironi, M., Mazzotta Epifani, E., Naletto, G., Palumbo, P., Eng, P., Roig, J.F., Caporali, A., Da Deppo, V., et al., 2010. SIMBIO-SYS: the spectrometer and imagers integrated observatory system for the BepiColombo planetary orbiter. Planet. Space Sci. 58 (1), 125–143. https://doi.org/10.1016/j.pss.2009.06.017.

Garzelli, A., 2014. Efficient MMSE pansharpening based on non-local optimization. 2014 IEEE Geoscience and Remote Sensing Symposium, pp. 195–198. https://doi.org/10.1109/IGARSS.2014.6946390.

Garzelli, A., 2016. A review of image fusion algorithms based on the super-resolution paradigm. Rem. Sens. 8 (10). https://doi.org/10.3390/rs8100797. Articolo 10.

Garzelli, A., Nencini, F., Capobianco, L., 2008. Optimal MMSE Pan sharpening of very high resolution multispectral images. IEEE Trans. Geosci. Rem. Sens. 46 (1), 228–236. https://doi.org/10.1109/TGRS.2007.907604.

Hallada, W.A., Cox, S., 1983. Image sharpening for mixed spatial and spectral resolution satellite systems. Int. Symposium Remote Sensing Environ. Proceedings of the International Symposium on Remote Sensing of Environment, Vol. 17, 1023-1024. https://ntrs.nasa.gov/search.jsp?R=19850028100.

Haydn, R., 1982. Application of the IHS color transform to the processing of multisensor data and image enhancement. In: Proc. Of the International Symposium on Remote Sensing of Arid and Semi-arid Lands, p. 198. Cairo, Egypt.

He, L., Zhu, J., Li, J., Plaza, A., Chanussot, J., Li, B., 2019. HyperPNN: hyperspectral pansharpening via spectrally predictive convolutional neural networks. IEEE J. Sel. Top. Appl. Earth Obs. Rem. Sens. 12 (8), 3092–3100. https://doi.org/10.1109/JSTARS.2019.2917584.

Huang, W., Xiao, L., Wei, Z., Liu, H., Tang, S., 2015. A new Pan-Sharpening method with deep neural networks. Geosci. Rem. Sens. Lett. IEEE 12 (5), 1037–1041. https://doi.org/10.1109/lgrs.2014.2376034.

Jin, C., Deng, L.-J., Huang, T.-Z., Vivone, G., 2022. Laplacian pyramid networks: a new approach for multispectral pansharpening. Inf. Fusion 78, 158–170. https://doi.org/10.1016/j.inffus.2021.09.002.

Kaur, G., Saini, K.S., Singh, D., Kaur, M., 2021. A comprehensive study on computational pansharpening techniques for remote sensing images. Arch. Comput. Methods Eng. 28 (7), 4961–4978. https://doi.org/10.1007/s11831-021-09565-y.

Kirk, R.L., Howington-Kraus, E., Rosiek, M.R., Anderson, J.A., Archinal, B.A., Becker, K. J., Cook, D.A., Galuszka, D.M., Geissler, P.E., Hare, T.M., Holmberg, I.M., Keszthelyi, L.P., Redding, B.L., Delamere, W.A., Gallagher, D., Chapel, J.D., Eliason, E.M., King, R., McEwen, A.S., 2008. Ultrahigh resolution topographic mapping of Mars with MRO HiRISE stereo images: meter-scale slopes of candidate Phoenix landing sites. J. Geophys. Res.: Planets 113 (E3). https://doi.org/10.1029/2007JE003000, 2007JE003000.

Kwan, C., Ayhan, B., Budavari, B., 2017. Fusion of themis and TES for accurate Mars surface characterization. IEEE Int. Geosci. Remote Sensing Symposium (IGARSS). https://doi.org/10.1109/igarss.2017.8127723.

Laben, C.A., Brower, B.V., 2000. Process for enhancing the spatial resolution of multispectral imagery using pan-sharpening. U.S. Patent 6, 011 875.

Laura, J., Acosta, A., Addair, T., Adoram-Kershner, L., Alexander, J., Alexandrov, O., Alley, S., Anderson, D., Anderson, J., Anderson, J., Annex, A., Archinal, B., Austin, C., Backer, J., Barrett, J., Bauck, K., Bauers, J., Becker, K., Becker, T., et al., 2023. Integrated Software for Imagers and Spectrometers (7.2.0RC1). Zenodo. https://doi.org/10.5281/zenodo.7644616.

Li, S., Yang, B., 2011. A new Pan-Sharpening method using a compressed sensing technique. IEEE Trans. Geosci. Rem. Sens. 49 (2), 738–746. https://doi.org/10.1109/tgrs.2010.2067219.

Li, X., Chen, H., Zhou, J., Wang, Y., 2020. Improving component substitution pan-sharpening through refinement of the injection detail. Photogramm. Eng. Rem. Sens. 86 (5), 317–325. https://doi.org/10.14358/PERS.86.5.317.

Liu, J.G., 2000. Smoothing Filter-based Intensity Modulation: a spectral preserve image fusion technique for improving spatial details. Int. J. Rem. Sens. 21 (18), 3461–3472. https://doi.org/10.1080/014311600750037499.

Loncan, L., de Almeida, L.B., Bioucas-Dias, J.M., Briottet, X., Chanussot, J., Dobigeon, N., Fabre, S., Liao, W., Licciardi, G.A., Simões, M., Tourneret, J.-Y., Veganzones, M.A., Vivone, G., Wei, Q., Yokoya, N., 2015. Hyperspectral pansharpening: a review. IEEE Geosci. Remote Sensing Magazine 3 (3), 27–46. https://doi.org/10.1109/MGRS.2015.2440094.

Lowe, D., 1999. Object recognition from local scale-invariant features. Proceedings of the Seventh IEEE International Conference on Computer Vision, Kerkyra, Greece. https://doi.org/10.1109/iccv.1999.790410.

Loizeau, D., Mangold, N., Poulet, F., Bibring, J.-P., Gendrin, A., Ansan, V., Gomez, C., Gondet, B., Langevin, Y., Masson, P., Neukum, G., 2007. Phyllosilicates in the Mawrth Vallis region of Mars. J. Geophys. Res.: Planets 112 (E8). https://doi.org/10.1029/2006JE002877.

Lucchetti, A., Pajola, M., Poggiali, G., Semenzato, A., Munaretto, G., Cremonese, G., Brucato, J.R., Massironi, M., 2021. Volatiles on Mercury: the case of hollows and the pyroclastic vent of Tyagaraja crater. Icarus 370, 114694. https://doi.org/10.1016/j.icarus.2021.114694.

Malin, M.C., Danielson, G.E., Ingersoll, A.P., Masursky, H., Veverka, J., Ravine, M.A., Soulanille, T.A., 1992. Mars observer camera. J. Geophys. Res.: Planets 97, 7699–7718. https://doi.org/10.1029/92JE00340.

Mastani, S.A., Shilpa, K., 2013. New approach of estimating PSNR-B for de-blocked images. arXiv (Cornell University). https://doi.org/10.48550/arXiv.1306.5293 abs/1306.5293.

Maurer, T., 2013. How to pan-sharpen images using the Gram-Schmidt pan-sharpen method—a recipe. ISPRS - International Archives of the Photogrammetry, Remote Sensing Spatial Info. Sci. XL-1/W1, 239–244. https://doi.org/10.5194/isprsarchives-XL-1-W1-239-2013.

McEwen, A.S., Eliason, E.M., Bergstrom, J.W., Bridges, N.T., Hansen, C.J., Delamere, W. A., Grant, J.A., Gulick, V.C., Herkenhoff, K.E., Keszthelyi, L., Kirk, R.L., Mellon, M.T., Squyres, S.W., Thomas, N., Weitz, C.M., 2007. Mars reconnaissance orbiter's high resolution imaging science experiment (HiRISE). J. Geophys. Res.: Planets 112 (E5). https://doi.org/10.1029/2005JE002605.

Meng, X., Xiong, Y., Shao, F., Shen, H., Sun, W., Yang, G., Yuan, Q., Fu, R., Zhang, H., 2021. A large-scale benchmark data set for evaluating pansharpening performance: Overview and implementation. IEEE Geosci. Remote Sensing Magazine 9 (1), 18–52. https://doi.org/10.1109/MGRS.2020.2976696.

Murchie, S., Arvidson, R., Bedini, P., Beisser, K., Bibring, J.-P., Bishop, J., Boldt, J., Cavender, P., Choo, T., Clancy, R.T., Darlington, E.H., Des Marais, D., Espiritu, R., Fort, D., Green, R., Guinness, E., Hayes, J., Hash, C., Heffernan, K., et al., 2007. Compact reconnaissance imaging spectrometer for Mars (CRISM) on Mars reconnaissance orbiter (MRO). J. Geophys. Res.: Planets 112 (E5). https://doi.org/10.1029/2006JE002682.

Palubinskas, G., 2013. Fast, simple, and good pan-sharpening method. J. Appl. Remote Sens. 7 (1), 073526. https://doi.org/10.1117/1.JRS.7.073526.

Parente, C., Pepe, M., 2017. Influence of the weights in IHS and Brovey methods for pan-sharpening WorldView-3 satellite images. IJET 6, 71. https://doi.org/10.14419/ijet.v6i3.7702.

Perry, J.E., Heyd, R., Read, M., Tornabene, L.L., Sutton, S.S., Byrne, S., Thomas, N., Fennema, A., McEwen, A., Berry, K., 2022. Geometric processing of TGO CaSSIS

observations. Planet. Space Sci. 223, 105581. https://doi.org/10.1016/j.pss.2022.105581.
Phillips, M.S., Viviano, C.E., Moersch, J.E., Rogers, A.D., McSween, H.Y., Seelos, F.P., 2022. Extensive and ancient feldspathic crust detected across north Hellas rim, Mars: possible implications for primary crust formation. Geology 50 (10), 1182–1186. https://doi.org/10.1130/G50341.1.
Pommerol, A., Thomas, N., Almeida, M., Read, M., Becerra, P., Cesar, C., Valantinas, A., Simioni, E., McEwen, A.S., Perry, J., Marriner, C., Munaretto, G., Pajola, M., Tornabene, L., Mège, D., Da Deppo, V., Re, C., Cremonese, G., 2022. In-flight radiometric calibration of the ExoMars TGO colour and stereo surface imaging system. Planet. Space Sci. 223, 105580. https://doi.org/10.1016/j.pss.2022.105580.
Ranchin, T., Wald, L., 2000. Fusion of High Spatial and Spectral Resolution Images: the ARSIS Concept and its Implementation. HAL (Le Centre Pour La Communication Scientifique Directe). https://hal.archives-ouvertes.fr/hal-00356168.
Re, C., Fennema, A., Simioni, E., Sutton, S., Mège, D., Gwinner, K., Józefowicz, M., Munaretto, G., Pajola, M., Petrella, A., Pommerol, A., Cremonese, G., Thomas, N., 2022. CaSSIS-based stereo products for Mars after three years in orbit. Planet. Space Sci. 219, 105515. https://doi.org/10.1016/j.pss.2022.105515.
Re, C., Tulyakov, S., Simioni, E., Mudric, T., Cremonese, G., Thomas, N., 2019. Performance evaluation of 3DPD, the photogrammetric pipeline for the CaSSIS stereo images. Int. Arch. Photogram. Rem. Sens. Spatial Inf. Sci. XLII-2/W13, 1443–1449. https://doi.org/10.5194/isprs-archives-XLII-2-W13-1443-2019.
Scarpa, G., Ciotola, M., 2022. Full-resolution quality assessment for pansharpening. Rem. Sens. 14 (8). https://doi.org/10.3390/rs14081808. Articolo 8.
Semenzato, A., Massironi, M., Ferrari, S., Galluzzi, V., Rothery, D.A., Pegg, D.L., Pozzobon, R., Marchi, S., 2020. An Integrated Geologic map of the Rembrandt Basin, on Mercury, as a starting point for stratigraphic analysis. Rem. Sens. 12 (19), 3213. https://doi.org/10.3390/rs12193213.
Shettigara, V.K., 1992. A generalized component substitution technique for spatial enhancement of multispectral images using a higher resolution data set. Photogramm. Eng. Rem. Sens. 58 (5), 561–567. http://pascal-francis.inist.fr/vibad/index.php?action=getRecordDetail&idt=5332292.
Thomas, C., Ranchin, T., Wald, L., Chanussot, J., 2008. Synthesis of multispectral images to high spatial resolution: a critical review of fusion methods based on remote sensing physics. IEEE Trans. Geosci. Rem. Sens. 46 (5), 1301–1312. https://doi.org/10.1109/TGRS.2007.912448.
Thomas, N., Cremonese, G., Ziethe, R., Gerber, M., Brändli, M., Bruno, G., Erismann, M., Gambicorti, L., Gerber, T., Ghose, K., Gruber, M., Gubler, P., Mischler, H., Jost, J., Piazza, D., Pommerol, A., Rieder, M., Roloff, V., Servonet, A., et al., 2017. The colour and stereo surface imaging system (CaSSIS) for the ExoMars Trace Gas orbiter. Space Sci. Rev. 212 (3–4), 1897–1944. https://doi.org/10.1007/s11214-017-0421-1.
Tornabene, L.L., Seelos, F.P., Pommerol, A., Thomas, N., Caudill, C.M., Becerra, P., Bridges, J.C., Byrne, S., Cardinale, M., Chojnacki, M., Conway, S.J., Cremonese, G., Dundas, C.M., El-Maarry, M.R., Fernando, J., Hansen, C.J., Hansen, K., Harrison, T. N., Henson, R., Wray, J.J., 2018. Image simulation and assessment of the colour and spatial capabilities of the colour and stereo surface imaging system (CASSIS) on the ExoMars Trace Gas orbiter. Space Sci. Rev. 214 (1). https://doi.org/10.1007/s11214-017-0436-7.
Tu, T., Hsu, C., Tu, P., Lee, C., 2012. An adjustable Pan-Sharpening approach for IKONOS/QuickBird/GeoEye-1/WorldView-2 imagery. IEEE J. Sel. Top. Appl. Earth Obs. Rem. Sens. 5 (1), 125–134. https://doi.org/10.1109/jstars.2011.2181827.
Vicinanza, M.R., Restaino, R., Vivone, G., Mura, M.D., Chanussot, J., 2015. A pansharpening method based on the sparse representation of injected details. Geosci. Rem. Sens. Lett. IEEE 12 (1), 180–184. https://doi.org/10.1109/lgrs.2014.2331291.
Vivone, G., Alparone, L., Chanussot, J., Dalla Mura, M., Garzelli, A., Licciardi, G.A., Restaino, R., Wald, L., 2015. A critical comparison among pansharpening algorithms. IEEE Trans. Geosci. Rem. Sens. 53 (5), 2565–2586. https://doi.org/10.1109/TGRS.2014.2361734.
Vivone, G., Dalla Mura, M., Garzelli, A., Restaino, R., Scarpa, G., Ulfarsson, M.O., Alparone, L., Chanussot, J., 2021. A new benchmark based on recent advances in multispectral pansharpening: revisiting pansharpening with classical and emerging pansharpening methods. IEEE Geosci. Remote Sensing Magazine 9 (1), 53–81. https://doi.org/10.1109/MGRS.2020.3019315.
Vivone, G., Restaino, R., Mura, M.D., Licciardi, G., Chanussot, J., 2014. Contrast and Error-Based fusion schemes for multispectral image pansharpening. Geosci. Rem. Sens. Lett. IEEE 11 (5), 930–934. https://doi.org/10.1109/lgrs.2013.2281996.
Wald, L., 2002. Data Fusion. Definitions and Architectures - Fusion of Images of Different Spatial Resolutions. Presses de l'Ecole, Ecole des Mines de Paris, Paris, France, p. 200. ISBN 2-911762-38-X. ⟨hal-00464703⟩.
Wald, L., Ranchin, T., Mangolini, M., 1997. Fusion of satellite images of different spatial resolutions: Assessing the quality of resulting images. Photogram. Eng. Rem. Sens. 63 (6), 691–699. https://hal.science/hal-00365304.
Wang, Z., Bovik, A.C., 2002. A universal image quality index. IEEE Signal Process. Lett. 9 (3), 81–84. https://doi.org/10.1109/97.995823.
Wang, Z., Bovik, A.C., Sheikh, H.R., Simoncelli, E.P., 2004. Image quality assessment: from error visibility to structural similarity. IEEE Trans. Image Process. 13 (4), 600–612. https://doi.org/10.1109/TIP.2003.819861.
Wei, Q., Bioucas-Dias, J., Dobigeon, N., Tourneret, J.-Y., 2015. Hyperspectral and multispectral image fusion based on a sparse representation. IEEE Trans. Geosci. Rem. Sens. 53 (7), 3658–3668. https://doi.org/10.1109/TGRS.2014.2381272.
Xie, W., Cui, Y., Li, Y., Lei, J., Du, Q., Li, J., 2021. HPGAN: hyperspectral pansharpening using 3-D generative adversarial networks. IEEE Trans. Geosci. Rem. Sens. 59 (1), 463–477. https://doi.org/10.1109/TGRS.2020.2994238.
Xu, R., Zhang, H., Wang, T., Lin, H., 2017. Using pan-sharpened high resolution satellite data to improve impervious surfaces estimation. Int. J. Appl. Earth Obs. Geoinf. 57, 177–189. https://doi.org/10.1016/j.jag.2016.12.020.
Yim, C., Bovik, A.C., 2011. Quality assessment of deblocked images. IEEE Trans. Image Process. 20 (1), 88–98. https://doi.org/10.1109/tip.2010.2061859.
Yuhas, R.H., Goetz, A.F.H., Boardman, J.W., 1992. Discrimination among semi-arid landscape endmembers using the Spectral Angle Mapper (SAM) algorithm. JPL, Summaries Third Ann. JPL Airborne Geosci. Workshop 1. AVIRIS Workshop - N. 94N16711. https://ntrs.nasa.gov/citations/19940012238.
Zhang, J., 2010. Multi-source remote sensing data fusion: status and trends. Int. J. Image Data Fusion 1 (1), 5–24. https://doi.org/10.1080/19479830903561035.